Master's Thesis

Thermoelectric properties of low-dimensional semiconductors

Nguyen Tuan Hung

Department of Physics
Graduate School of Science
Tohoku University

September, 2016

Acknowledgments

I would like to use this opportunity to thank the many people who contributed to this thesis over the two years of my master course study at Tohoku University. First of all, I am very grateful to my supervisor, Professor Riichiro Saito, for his teaching me fundamentals of research, basic ideas in solid state physics, proper English usage, and also scientist attitudes. I really appreciate his patience with my bad language ability and my bad understanding of even simple facts in physics. He has also inspired me to pursue physics with many new insights and thoughts, which I have never learned before. I would like to thank our collaborator Professor Mildred S. Dresselhaus (MIT) for her kind advices for thermoelectricity. I would like to express my gratitude to Dr. A. R. T. Nugraha for teaching me (again) proper English usage and physics. He is also a very important co-advisor. For all of my lab mates: Hasdeo-san, Pourya-san, Shoufie-san, Inoue-san, Shirakura-san, Tatsumi-san, it has been a great time to work with you all.

I am very thankful to Interdepartmental Doctoral Degree Program for Multidimensional Materials Science Leaders in Tohoku University for financially supporting my study. Finally, above all else, I would like to say thank you to my family whom unwavering love carries me through all of life's adventures. No matter what happens, they are always there. I would especially appreciate a woman who give the meaning to my life, Trang, my lovely wife who is the most gentle and loyal woman I have ever seen. Her endless love and support make the every moment of my life give me motivation to make our life happier.

Abstract

Although thermoelectricity is considered an old subject, recently the research on thermoelectricity has been very active due to the desire to achieve a very efficient thermoelectric device for energy generation from heat waste. Thanks to nanotechnology, this effort is expected to be possible in the near future by miniaturization of solid-state materials. The efficiency of a solid-state thermoelectric power generator is usually evaluated by the dimensionless figure of merit, $ZT = S^2\sigma\kappa^{-1}T$, where S is the Seebeck coefficient, σ is the electrical conductivity, κ is the thermal conductivity, and T is the absolute temperature. Traditionally, high ZT has been the only parameter pursued to obtain good thermoelectric materials. However, the importance of maximizing the power factor, $PF = S^2\sigma$, can be recognized from the fact that when the heat source is unlimited [PNAS 112 (2015) 3269], the ZT value is no longer the only parameter to judge the thermoelectric efficiency. We thus would like to consider the issue of maximizing PF as the main topic of this thesis, especially for semiconducting materials which are basically better than insulating or metallic materials to maximize their PF. We further consider semiconducting single wall carbon nanotubes (s-SWNTs) as a good candidate of thermoelectric materials.

To optimize thermoelectric power factor PF of semiconducting materials, here we theoretically investigate the interplay between the confinement length L and the thermal de Broglie wavelength Λ to optimize the thermoelectric power factor of semiconducting materials. An analytical formula for the power factor is derived based on the one-band model assuming nondegenerate semiconductors to describe quantum effects on the power factor of the low dimensional semiconductors. The power factor is enhanced for one- and two-dimensional semiconductors when L is smaller than Λ of the semiconductors. In this case, the low-dimensional semiconductors having L smaller than their Λ will give a better thermoelectric performance compared to their bulk counterpart. On the other hand, when L is larger than Λ, bulk semiconductors may give a higher power factor compared to the lower dimensional ones.

One step towards realizing high PF is be optimizing the thermopower (or the Seebeck coefficient), especially for one-dimensional materials such as semiconducting single wall carbon nanotubes (s-SWNTs). Since electrical properties are very sensitive to each s-SWNTs structure. Therefore, we calculate the thermopower for many

s-SWNTs within a diameter range of 0.5–1.5 nm by using the Boltzmann transport theory combined with an extended tight-binding model. We find that the thermopower of the s-SWNTs increases as the tube diameter decreases. For the small s-SWNT with diameter less than 0.6 nm, the thermopower can reach a value of 2000 V/K, which is about 6–10 times larger than commonly used semiconducting materials in thermoelectric applications. We derive a simple formula to reproduce the numerical calculation and we find that the thermopower of the s-SWNTs has a band gap term, which explains the shape of the thermopower plot as a function of diameter. Interestingly, this plot looks very similar to the so-called Kataura plot for optical transition for s-SWNTs, showing the $2n + m$ family pattern. It should be noted that the Kataura plot was a fundamental work based on the optical properties of SWNTs. Our results highlight potential properties of small diameter s-SWNT as a one-dimensional thermoelectric material with a large thermopower.

Contents

Chapter 1

Introduction

1.1 Purpose of the study

More than 90% of the energy we use in daily life comes from thermal processes, such as the heat engines in most of cars and power plants, in which more than half of the energy is wasted in form of heat [1]. Research for recovering this waste heat are thus of great interest, particularly at times when there is a high demand for renewable energy with the necessity of reducing carbon emission. This research field is known as thermoelectricity, which is a study of how one can convert waste heat directly into electric energy [2, 3]. A good thermoelectric material is characterized by how efficient electricity can be obtained for a given heat input, where two parameters are usually evaluated: (1) power factor ($PF = S^2\sigma$, where S is the thermopower and σ is the electrical conductivity) and (2) thermoelectric figure-of-merit ($ZT = PF \times T/\kappa$, where PF is the power factor, T is the absolute temperature, and κ is the thermal conductivity). [4, 5]. In applications where the heat source is essentially free (e.g., solar thermal, nuclear power, or waste-heat recovery from cars), the minimum overall cost of generating power is achieved by operating at maximum PF. On the other hand, when heat source is costly (e.g., fossil fuel combustion), obtaining as large ZT as possible is important to reduce the cost of generating power [6].

A previous theoretical study by Hicks and Dresselhaus in 1993 predicted that the smaller confinement length of a material, such as the thickness in thin films and the diameter in nanowires, could increase the PF and the ZT of low-dimensional structures [7, 8]. However, there have been some recent experiments which showed that PF of one-dimensional (1D) Si nanowires is still similar to that of the 3D bulk system [9, 10], while other experiments on Bi nanowires show an enhanced PF value compared to its bulk state [11]. The origin of the discrepancy that depends on materials is not explained yet. Therefore, the purpose of this thesis is to solve the issue of maximizing themoelectric power factor in low-dimensional materials by considering

an additional parameter of material to enhance the power factor. Moreover, we also study a possibility of using semiconducting carbon nanotubes as a good candidate of thermoelectric materials. Carbon nanotubes are selected in this thesis due to a lot of variety of their geometrical structure which allows us to find excellent physical properties that we desire [12].

1.2 Organization

This thesis is organized into five chapters. Chapters 1 and 2 form basic information of this thesis. In Chapter 1, we explain the purpose and the background of the study. In Chapter 2, we review the fundamentals of transport properties of low-dimensional semiconductors and explain the methods we use in this study, the so-called one-band and two-band models. We also give electronic structure of graphene and carbon nanotubes using extended tight-binding (ETB) approximation. The thermopower and the electrical conductivity are calculate based on the one-band and two-band models. The main results of this thesis are presented in Chapters 3 and 4. In Chapter 3, we show calculation results for the thermoelectric power factor of low-dimensional materials. In Chapter 4 we show calculated results for the thermopower of semiconducting single wall carbon nanotubes (s-SWNTs). Finally, in Chapter 5, a summary of this thesis is given.

1.3 General backgrounds

In this section, we review some important backgrounds in the thermoelectric field that motivate the present work. We will examine the fundamental effects of thermoelectricity including the Seebeck effect and the Peltier effect. Then, we show some general concepts on thermoelectric devices, such as the power factor PF, the figure-of-merit ZT, and the output power density Q. The problems to improve thermoelectric power factor of low-dimensional semiconductor will also be discussed briefly.

1.3.1 Thermoelectric effects

Thermoelectric devices are designed based on two fundamental thermoelectric effects, namely the Seebeck effect and the Peltier effect. The Seebeck effect was first observed in 1821 by a German physicist, Thomas Johann Seebeck. It is thus not surprising that the thermoelectric coefficient is called as the Seebeck coefficient S, but often it is also referred to as thermoelectric power (TEP) or thermopower. All of these names correspond to the same thermoelectric property of a material. Hereafter, for convenience and simplicity, we will use the term *thermopower* for referring to the Seebeck effect. The thermopower is defined by how much voltage difference, ΔV,

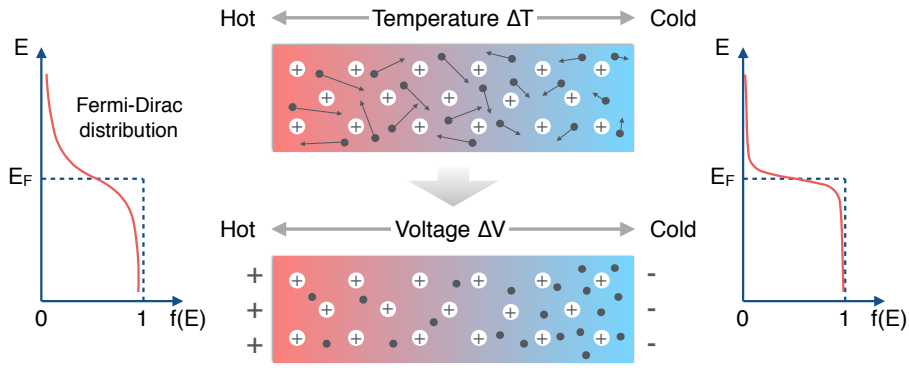

Figure 1.1: Seebeck effect illustration.

develops in response to the applied temperature gradient ΔT. The thermopower can be mathematically expressed as

$$S = -\frac{\Delta V}{\Delta T}. \tag{1.1}$$

The units of thermopower is volts per kelvin (V/K) in SI units.

The origin of the voltage in the Seebeck effect can be understood in the following simple explanation. Imagine a semiconductor (or metal) wire whose one end is kept in a cold source and the other in a hot source, as shown in Fig. 1.1. There is a high electronic charge distribution at the hot edge based on the Fermi-Dirac distribution function. In contrast, there is low electronic charge distribution at the cold edge. In addition, the electronic charges at the hot edge have higher energy, especially kinetic energy (KE), since the averaged value of $KE = \frac{3}{2}k_{\mathrm{B}}T$ for an ideal gas, where k_{B} is the Boltzmann constant and T is the absolute temperature. The electronic charges are thus very agile than those at the cold edge. Therefore, by having a temperature gradient ΔT from an edge of a semiconductor wire to its another edge, charge carriers (electrons or holes) will flow from the hot edge to the cold edge, which generates a voltage difference ΔV in the semiconductor wire [Fig. 1.1]. However, if the both electron and hole moves in the same direction, we do not get the current. Thermoelectric devices are thus made by two types (n-type and p-type) of semiconductor [Fig. 1.2].

The second thermoelectric effect, which is the inverse of the Seebeck effect, was discovered in 1834 by a French watchmaker Jean Peltier. While the Seebeck effect occurs in a single wire of conducting material, the Peltier effect is observed when two different conductors are brought together at a junction. By passing a direct current I through the two junctions, it can create a temperature difference. This efffect may sound similar to Joule heating, which is the generation of heat by passing an electric current through a metal, but in fact it is not. In Joule heating the current is only

Fig. 1.1: Fig/chapter1-fig1.pdf

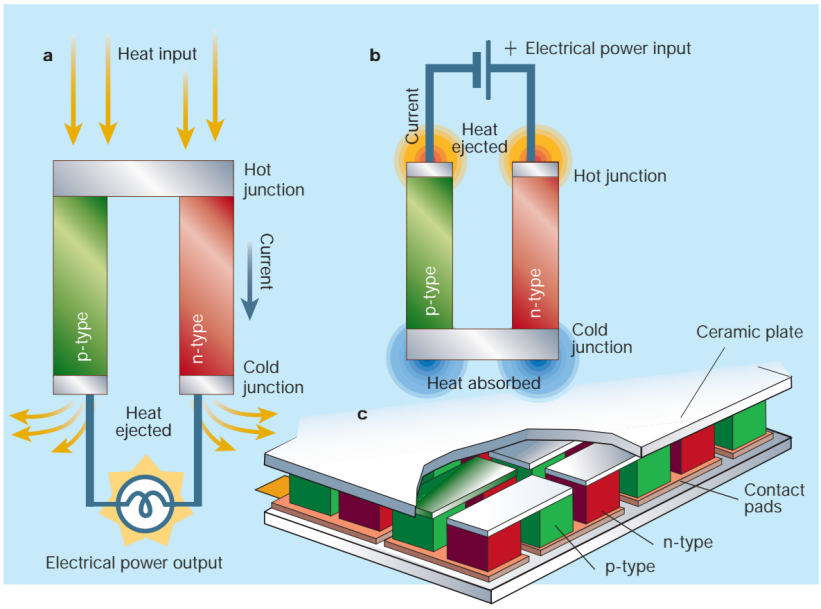

Figure 1.2: Thermoelectric devices are shown, configured for (a) power generation (Seebeck effect) or (b) refrigeration (Peltier effect). Thermocouple is a simple thermoelectric device including both the n-type and p-type semiconductors that are connected in series. (c) State-of-the-art thermoelectric modules can contain up to several thousand individual thermocouples. (Graphics of S. Williams, www.thermoelectrics.com.)

increasing the temperature in the material in which it flows. However, in Peltier effect devices, a temperature difference is created, i.e., one junction becomes cooler and one junction becomes hotter. Generation of heat Q occurs at the two junctions depending on the direction of the electric current. The Peltier coefficient, Π, is defined by [13]

$$\Pi = -\frac{Q}{I}. \tag{1.2}$$

The units of the Peltier coefficients is the volts (V) in SI units. The Seebeck and Peltier coefficients are related by the Kelvin relationship [13]

$$\Pi = ST, \tag{1.3}$$

which can be derived by applying irreversible thermodynamics [13].

The Seebeck effect is the basis for power-generation devices and the Peltier effect is the basis for many modern-day refrigeration devices. The devices are not using only one semiconductor "legs"; they use two types (n-type and p-type) of semiconductor that are connected in series (thermocouple), as shown in Figs. 1.2 (a) and (b).

Fig. 1.2: Fig/chapter1-fig2.pdf

Negatively charged electrons carry electrical current in the n-type leg, whereas positively charged holes carry the current in the p-type leg. A thermoelectric module is built up of an array of these couples, arranged electrically in series and thermally in parallel [14], as shown in Fig. 1.2 (c).

1.3.2 Output power density Q and figure of merit ZT

Thermoelectric generators should be operated at maximum power or maximum efficiency. In applications where the heat source is essentially free (e.g., solar heat, nuclear power, or waste-heat from cars), the minimum cost of generating total power is achieved by operating at maximum power [6]. On the other hand, when heat source is costly (e.g., fossil fuel combustion), the maximum efficiency is important to reduce the cost of generating power. For maximizing power or efficiency, it is required that one should optimize the electrical power density Q or the figure of merit ZT, respectively.

The electrical power P_{out} on the Joule heat delivered to the load [see in Fig. 1.2 (a)] is given by

$$P_{\text{out}} = I^2 R_L, \tag{1.4}$$

where I is the electric current and R_L is the resistance of the load. The units of P_{out} is the watt (W) in SI units. Within the constant property model approximation (CPM), and ignoring thermal and electrical contact resistance, the current I is induced by the Seebeck effect

$$I = \frac{S(T_h - T_c)}{R_L + R}, \tag{1.5}$$

where, $S = S_p - S_n$ and $R = R_p + R_n$ represent the Seebeck coefficient and resistivity of the thermocouple (p-type and n-type legs) of the thermoelectric device. T_h and T_c are the temperatures at the hot and cold sites, respectively. It should be noted that S and R are constants in the CPM, and T_h and T_c are given by the boundary condition. We can now determine the maximum output power as a function of R_L from Eqs. (1.4) and (1.5) by solving $\mathrm{d}(P)/\mathrm{d}(R_L) = 0$. The maximum out power, P_{max}, is found to be

$$P_{\text{max}} = \frac{1}{4}\frac{S^2(T_h - T_c)^2}{R}, \tag{1.6}$$

whereas the corresponding value for the load resistance is $R_L = R$. The electrical resistance of the thermocouple ($R = h_l/\sigma A$) can be written in terms of the thermocouple geometry (total cross-sectional area of n-type and p-type legs $A = A_p + A_n$ and leg length $h_l = h_p = h_n$) and the electrical conductivity, $\sigma = \sigma_p\sigma_n/(\sigma_p + \sigma_n)$, of the thermocouple. Equation (1.6) can then be rewritten as

$$P_{\text{max}} = \frac{1}{4h_l} S^2 \sigma (T_h - T_c)^2 A. \tag{1.7}$$

Equation (1.7) also contains the power factor $PF = S^2\sigma$. This results in an expression for out power density as

$$Q = \frac{P_{\max}}{A} = \frac{1}{4h_l} PF(T_h - T_c)^2, \tag{1.8}$$

The units of Q is the watt per unit area of the thermocouple ($\mathrm{W/m^2}$). Equation (1.8) shows that high PF is required for optimizing Q. It is note that decreasing the leg length also increases the output power density.

Let us now consider the heat flow into the hot side, P_{in}, consists of three components. They are: (1) the heat flow through the thermoelectric material due to the thermal conductance of the material (P_{cond}), (2) the absorbed heat at the hot junction due to the Peltier effect (P_{Pelt}), and (3) the heat that arrives at the hot side due to Joule heating of the thermocouple under the assumption that half of this heat goes to the hot side and half to the cold side (P_{Joule}). We can write as

$$P_{\text{in}} = P_{\text{cond}} + P_{\text{Pelt}} - P_{\text{Joule}} = \kappa \frac{A}{l_h}(T_h - T_c) + SIT_h - \frac{1}{2} I^2 R, \tag{1.9}$$

where $\kappa = \kappa_p \kappa_n / (\kappa_p + \kappa_n)$ is the thermal conductivity of the thermocouple (p-type and n-type legs).

Since the output power and the input power are both known, the efficiency can be computed. The efficiency η of a thermoelectric generation device is measured as the ratio of output power delivered to the load (P_{out}) to the heat flow into the hot side of the thermocouple (P_{in}).

$$\eta = \frac{P_{\text{out}}}{P_{\text{in}}}. \tag{1.10}$$

In the case of maximum of power output ($P_{\max}$), and substituting Eqs. (1.6) and (1.9) into Eq. (1.10), η can be expressed as

$$\eta = \frac{T_h - T_c}{\dfrac{3T_h + T_c}{2} + \dfrac{4}{Z}}. \tag{1.11}$$

where Z is given by

$$Z = \frac{S^2\sigma}{\kappa}. \tag{1.12}$$

The quantity Z is intrinsically determined by the physical properties of the thermocouple. However, $R_L = R$ (in the case of $P_{\max}$) is not the condition for maximizing efficiency. If we denote $m = R_L/R$ and substituting Eqs. (1.4), (1.5), and (1.9) into Eq. (1.10), then η is generally expressed as

$$\eta = \frac{T_h - T_c}{T_h} \frac{\dfrac{m}{1+m}}{1 + \dfrac{1+m}{T_h Z} - \dfrac{T_h - T_c}{2T_h(1+m)}}. \tag{1.13}$$

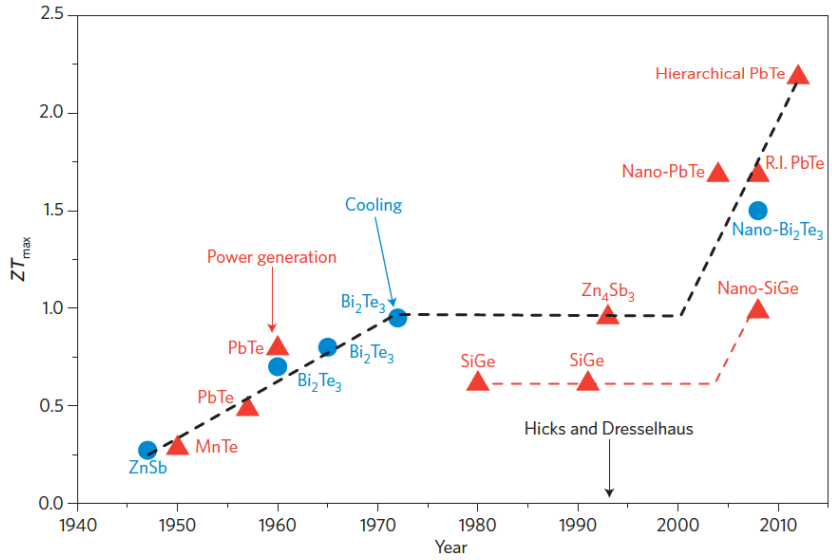

Figure 1.3: Evolution of the maximum ZT over time [Ref. [2]]. Materials for thermoelectric cooling are shown as blue dots and for thermoelectric power generation as red triangles. The material systems that have achieved $ZT > 1$ have been based on nanostructuring.

Now, η is a function of the temperatures at the hot and cold junctions, of Z, and of m. By solving $\mathrm{d}(\eta)/\mathrm{d}(m) = 0$, the maximum possible efficiency is given by

$$\eta_{\max} = \frac{T_h - T_c}{T_h} \frac{\sqrt{1+ZT}-1}{\sqrt{1+ZT}+\frac{T_h}{T_c}}, \tag{1.14}$$

whereas the corresponding value for m is $m = \sqrt{1+ZT}$. The average temperature T of the hot and cold side is defined by

$$T = \frac{T_h + T_c}{2}. \tag{1.15}$$

The unit of Z is (1/K), but the commonly used combined quantity ZT is dimensionless. It is then named the (dimensionless) figure-of-merit, which can be rewritten as

$$ZT = \frac{PF}{\kappa}T, \tag{1.16}$$

One realizes that the larger ZT is the higher efficiency. Equations (1.8) and (1.16) show that increasing the PF value is important to enhance not only Q but also ZT for power generation applications, respectively.

1.3.3 Low-dimensional thermoelectric energy conversion

Fig. 1.3: Fig/chapter1-fig3.pdf

The phenomenon of thermoelectricity was first observed by Thomas Johann Seebeck who noticed that when a loop was made from wires using two dissimilar metals, a voltage appeared between the junctions of the wires if one junction was hotter than the other. For over a century thermocouples were made from metallic conductors and though many different metals were investigated, efficiencies rarely exceeded 3%. The voltage generated by the metallic thermocouples are relatively small and it is not enough to make a practical thermoelectric generator. Following the development of semiconductors in the 1950s, it was found that replacing the metal wires with bulk semiconductors improved the efficiency of thermocouples by more than an order of magnitude. The commercial solid-state power generation systems using bulk semiconductors have long been the technology for the space missions, including the Voyager I and II probes to the outer planets and, more recently, the Cassini mission to Saturn. A big improvement, but normal thermoelectric technology would still cost too much and consume too much electricity to replace that conventional generators in industry.

With the introduction of low-dimensional materials and concepts based on nanostructuring, however, the thermoelectricity field has witnessed truly dramatic growth over the past 25 years. Heremans *et al.* [2] have shown the evolution of the thermoelectric efficiency, which is characterized by figure-of-merit ZT value, as a function of time as shown in Fig. 1.3. It is important to note that some material systems that have achieved high ZT values have been based on nanostructuring. A theoretical study by Hicks and Dresselhaus in 1993 predicted the potential benefits of low-dimensional materials to thermoelectrics in their seminal articles [7, 8] on the modeling of thermoelectric thin films and nanowires. In these structures, electrons are confined to a physical space with lower dimensions, and the resulting density of states exhibits sharp transitions with respect to energy, which is desirable for a high Seebeck coefficient. This quantum confinement effect was confirmed experimentally in 1996 using $PbTe/Pb_{1-x}Eu_xTe$, which exhibited a thermoelectric figure-of-merit value up to about five times greater than that of the corresponding bulk value [15]. It is thus intriguing to evaluate thermoelectricity in low-dimensional semiconductors that might have excellent thermoelectric performance, either theoretically or experimentally.

1.3.4 Importance of thermoelectric power factor

As has been explained before, the efficiency of a solid-state thermoelectric power generator is usually evaluated by the dimensionless figure of merit, $ZT = S^2\sigma\kappa^{-1}T$, as shown in Eq. (1.6). A fundamental aspect in the research of thermoelectricity is the demand to maximize the ZT value by having large S, high σ, and low κ. However, since the transport characteristics σ and κ are generally interdependent according to the Wiedemann-Franz law, it has always been challenging for researchers to find materials with $ZT > 2$ at room temperature [3, 16]. Huge efforts have been dedicated

to reduce κ using semiconducting materials with low-dimensional structures, in which κ is dominated by phonon heat transport. For example, recent experiments using Si nanowires have observed that κ can be reduced below the theoretical limit of bulk Si (0.99 W/mK) because the phonon mean free path is limited by boundary scattering in nanostructures [9, 10]. In these experiments, the reduction of the semiconducting nanowire diameter is likely to achieve a large enhancement in thermoelectric efficiency with $ZT > 1$ at room temperature [9, 10]. The success in reducing κ thus leads to the next challenge in increasing the thermoelectric power factor $PF = S^2\sigma$.

The importance of maximizing the PF can be recognized from the fact that when the heat source is unlimited, the ZT value is no longer the only one parameter to evaluate the thermoelectric efficiency. In this case, the output power density Q is also important to be evaluated [4, 5]. The PF term appears in the definition of Q, particularly for its maximum value, $Q_{\max} = PF(T_h - T_c)^2/4h_\ell$ [Eq. (1.8)]. Since the term $(T_h - T_c)^2/4h_\ell$ is given by the boundary condition, Q is mostly affected by PF.

Here we mention the definition of not PF but Q because some materials show high ZT but low thermoelectric performance due to their small Q. For example, Liu et al. [5] has compared two materials: PbSe (with maximum values of $ZT = 1.3$, $PF = 21$ μW/cmK^2) [18] and $Hf_{0.25}Zr_{0.75}NiSn$ ($ZT = 1$, $PF = 52$ μW/cmK^2) [18]. Both materials have similar cubic crystalline structure but the difference on their thermoelectric properties is obvious, as shown in Fig. 1.4 (a)–(e). First, the electrical conductivity and thermal conductivity of PbSe are lower than those of $Hf_{0.25}Zr_{0.75}NiSn$ because of the intrinsic resonant bonding of PbSe [19]. Second, PbSe has stronger temperature dependence of electrical conductivity and Seebeck coefficient compared with $Hf_{0.25}Zr_{0.75}NiSn$. At a given hot side temperature ($T_h = 500$ °C) and cold side temperatures ($T_c = 50$ °C) with a leg length ($h_\ell = 2$ mm) as the boundary conditions, PbSe ($Hf_{0.25}Zr_{0.75}NiSn$) has thermoelectric efficiency η [Eq. (1.14)] of about 11% (10%), as shown in Fig. 1.4 (f).

If the thermoelectric efficiency is the only concern, PbSe is definitely better than $Hf_{0.25}Zr_{0.75}NiSn$. However, $Hf_{0.25}Zr_{0.75}NiSn$ has much higher output power ($Q = 14.4$ W/cm^2) than that of the PbSe ($Q = 5.4$ W/cm^2) at same boundary conditions ($T_h = 500$ °C, $T_c = 50$ °C, $h_\ell = 2$ mm). From this information, we can see that although PbSe has a larger ZT, its output power is smaller than $Hf_{0.25}Zr_{0.75}NiSn$. Therefore, increasing the PF value is important to enhance not only ZT but also Q for power generation applications. We thus would like to consider the issue of maximizing PF as the main topic of this master thesis.

Fig. 1.4: Fig/chapter1-fig4.pdf

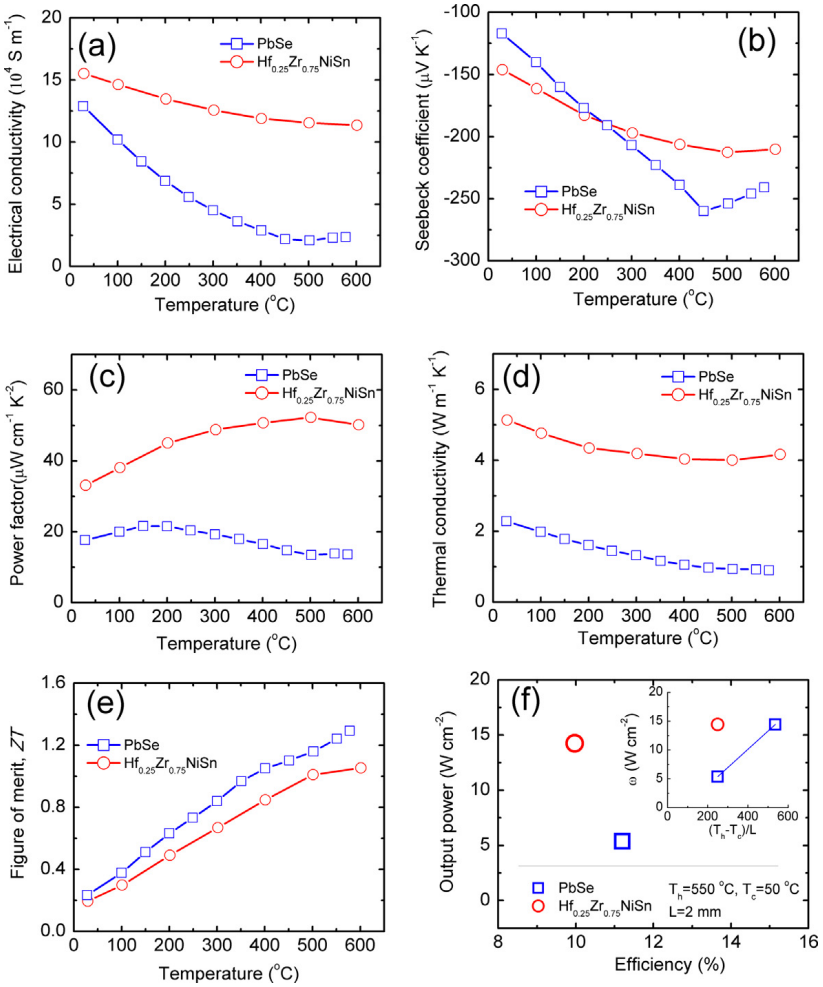

Figure 1.4: Comparison of thermoelectric properties between two reported thermoelectric materials: open circles are $Hf_{0.25}Zr_{0.75}NiSn$ [17] and open squares are PbSe [18]. (a) Temperature-dependent electrical conductivity σ. (b) Temperature-dependent Seebeck coefficient S. (c) Temperature-dependent power factor PF. (d) Temperature-dependent thermal conductivity κ. (e) Temperature-dependent figure-of-merit ZT. (f) Output power as function of efficiency.

1.3.5 Problems to improve thermoelectric power factor

Let us see some problems which arise when we want to improve thermoelectric power factor of a semiconducting material. First, one of the method to increase the value of thermoelectric power factor PF is the reduction of confinement length L, which is defined by the effective size of the electron wave functions in the non-principal direction for low-dimensional materials, such as the thickness in thin films or width in nanowires. This method might be the most straightforward technique since it was

proven to increase ZT [15, 10, 20, 11]. A theoretical study by Hicks and Dresselhaus in 1993 predicted that the smaller confinement length can increase PF and ZT of low-dimensional structures [7, 8], thanks to the quantum confinement effect to create sharp features in the density of states. However, if we look at some previous works more carefully into the subject of the confinement effects on the PF, there were some experiments which showed that the PF values of Si nanowires is still similar to that of the bulk values [9, 10], while other experiments on Bi nanowires show an enhanced PF values compared to its bulk state values [11]. This situation indicates that there is another parameter that can be compared with the confinement length. We will show in this thesis that the thermal de Broglie length Λ is a key parameter that defines the quantum effects in thermoelectricity. In order to show these effects, we investigate the quantum confinement effects on the PF for typical low-dimensional semiconductors. By comparing the confinement length with the thermal de Broglie length, we discuss the quantum effects and the classical limit on the PF, from which we can obtain an appropriate condition to maximize the power factor.

Second, one step towards realizing a high PF value is by optimizing the thermopower S (or the Seebeck coefficient), especially for one-dimensional materials such as semiconducting single-wall carbon nanotubes (s-SWNTs). As a low-dimensional material, SWNTs were considered to be promising for thermoelectric materials due to their one-dimensional electronic properties which depend on their geometrical structure [21, 22, 23]. Recent experiments [23, 24] have shown that s-SWNT network is capable of S values about 100–200 μV/K. However, the s-SWNT network samples have complex geometrical and electronic structures. The potential thermoelectric properties might have been lost because of connection between different tubes [21]. Such s-SWNT network samples consist of a collection of SWNTs with different diameters and chiralities, parameters to which the electronic structure is very sensitive [12]. Therefore, the thermopower values of the SWNT network samples were mainly attributed to S of both metallics and semiconductors, which might be a result of the increasing their thermopower. In this thesis, we will focus on evaluating the thermopower theoretically for a single s-SWNT with many diameters, and thus to maximize the SWNT thermopower and to suggest a new route for obtaining a larger PF for SWNTs. By calculating the thermopower of all individual s-SWNTs within a diameter range from 0.5 nm to 1.5 nm, we will show that, for tube diameters less than 0.6 nm, the thermopower of s-SWNTs can be as large as 2000 μV/K at room temperature, which is much large compared with the thermopower of bundled SWNTs, which is about 100–200 μV/K [23, 24]. From this result, we believe that there is still plenty of room to improve the PF of carbon nanotubes. For a more practical purpose, we also give an analytical formula to reproduce our numerical calculation of the s-SWNT thermopower, which forms a map of the s-SWNT thermopower. The calculated thermopower map could be useful for obtaining information on the s-SWNT chirality with a desired thermopower value

and thus it offers promise for using specially prepared s-SWNT samples to guide the direction of future research on the thermoelectricity.

Chapter 2

Theoretical methods

Physical properties of low-dimensional semiconductors, graphene, and single wall carbon nanotube are reviewed in this chapter. The discussion includes a description of the effective mass theorem, the band structure, and the density of state for the low-dimensional semiconductors. Then one-band model and two-band model for thermoelectricity are discussed based on the Boltzmann transport theory. The transport coefficients such as thermopower (or Seebeck coefficient) and electrical conductivity within the Boltzmann transport formalism are also discussed with in a tight-binding framework.

2.1 Energy band structure of low-dimensional structures

2.1.1 Effective mass theorem

Finding location of a particle in real space and its momentum at the same time is a fundamental variables in transport problem. To do that, the concept of a wave packet is necessary. A wave packet is a linear combination of the Bloch eigenstates, which have a finite spread both in the momentum and real space, for small region in the Brillouin zone (BZ). It is suitable for investigate properties of electrons and holes located very close to the band extrema points such as bottom of the conduction band (CB) or the top of the valence band (VB). Therefore, a wave packet is created by taking a linear combination of the Bloch eigenstates around such points in the **k**-space. The eigenstates of solid are Bloch functions for the n^{th} energy band with the wavevector **k**

$$\phi_{n\mathbf{k}}(\mathbf{r}) = e^{i\mathbf{k}\cdot\mathbf{r}} u_{n\mathbf{k}}(\mathbf{r}), \tag{2.1}$$

where $u_{n\mathbf{k}}$ is periodic function of the unit cell. The wave packet $\psi(\mathbf{r})$ can be written in terms of the Bloch states with over the whole BZ as

$$\psi(\mathbf{r}) = \sum_n \sum_{\mathbf{k}} A(\mathbf{k}) \phi_{n\mathbf{k}}(\mathbf{r}) = \sum_n \int \frac{\mathrm{d}(\mathbf{k})}{2\pi} A(\mathbf{k}) \phi_{n\mathbf{k}}(\mathbf{r}). \tag{2.2}$$

We now make two approximation:

1. The wavefunctions from only one band play in the wave packet. We can thus drop the sum over n in Eq. (2.2).

2. The wavevectors from a small region around $\mathbf{k}_0 = 0$ are important in this single band, and correspondingly expand the Bloch functions in Eq. (2.1)

$$\phi_{n\mathbf{k}}(\mathbf{r}) = e^{i\mathbf{k}\cdot\mathbf{r}} u_{n\mathbf{k}}(\mathbf{r}) \approx u_{n0} e^{i\mathbf{k}\cdot\mathbf{r}} = \phi_{n0}(\mathbf{r}) e^{i\mathbf{k}\cdot\mathbf{r}}. \tag{2.3}$$

With these approximations, the wave packet in Eq. (2.2) can be rewritten as

$$\psi(\mathbf{r}) = \sum_n \int \frac{\mathrm{d}(\mathbf{k})}{2\pi} A(\mathbf{k}) \phi_{n\mathbf{k}}(\mathbf{r}) = \phi_{n0}(\mathbf{r}) \int \frac{\mathrm{d}(\mathbf{k})}{2\pi} A(\mathbf{k}) e^{i\mathbf{k}\cdot\mathbf{r}} = \phi_{n0}(\mathbf{r}) F(\mathbf{r}), \tag{2.4}$$

where the integral term is identified as the Fourier transform from the weights $A(\mathbf{k})$ in $\mathbf{k}$-space to $F(\mathbf{r})$ in real space. The real-space function $F(\mathbf{r})$ is called as the envelope function. Since the weights $A(\mathbf{k})$ have a value in small region of $\Delta\mathbf{k}$ in the reciprocal space, the wave packet has a large spread in real space with $\Delta\mathbf{r} \sim 1/\Delta\mathbf{k}$. $F(\mathbf{r})$ is typically a smooth function spreading over several lattice constants.

When we apply the periodic Hamiltonian, H_0, of the crystal, let us start with the Bloch-eigenfunctions of H_0 to know the behavior of the wave packet

$$H_0 \phi_{n\mathbf{k}}(\mathbf{r}) = E_n(\mathbf{k}) \phi_{n\mathbf{k}}(\mathbf{r}), \tag{2.5}$$

and the Schrödinger equation for the wave packet is given by

$$H_0 \psi(\mathbf{r}) = \int \frac{\mathrm{d}(\mathbf{k})}{2\pi} A(\mathbf{k}) E_n(\mathbf{k}) \phi_{n\mathbf{k}}(\mathbf{r}). \tag{2.6}$$

It follows from Bloch's theorem that $E_n(\mathbf{k})$ is a periodic function in the reciprocal lattice. Therefore, $E_n(\mathbf{k})$ can be expanded by the Fourier series in the real space as

$$E_n(\mathbf{k}) = \sum_{\mathbf{R}_l} E_{nl} e^{i\mathbf{k}\cdot\mathbf{R}_l}, \tag{2.7}$$

where the $\mathbf{R}_l$ are lattice vector. Now consider Eq. (2.7) by replacing $\mathbf{k}$ by the differential operator $-i\vec{\nabla}$, we obtain

$$E_n(-i\vec{\nabla}) = \sum_{\mathbf{R}_l} E_{nl} e^{i\mathbf{R}_l \cdot \vec{\nabla}}. \tag{2.8}$$

Now consider the effect of the operator $-i\vec{\nabla}$ on an arbitrary function $f(\mathbf{r})$. Since $e^{\mathbf{R}_l \cdot \vec{\nabla}}$ can be expanded in a Taylor series as

$$\begin{aligned} e^{\mathbf{R}_l \cdot \vec{\nabla}} f(\mathbf{r}) &= \left[1 + \mathbf{R}_l \cdot \vec{\nabla} + \frac{1}{2!}(\mathbf{R}_l \cdot \vec{\nabla})(\mathbf{R}_l \cdot \vec{\nabla}) + \ldots\right] f(\mathbf{r}) \\ &= f(\mathbf{r}) + \mathbf{R}_l \cdot \vec{\nabla} f(\mathbf{r}) + \frac{1}{2} R_{l\alpha} R_{l\beta} \frac{\partial^2}{\partial r_\alpha \partial r_\beta} f(\mathbf{r}) + \ldots \\ &= f(\mathbf{r} + \mathbf{R}_l) \end{aligned} \quad . \tag{2.9}$$

Thus when we apply operator $-i\vec{\nabla}$ to a Bloch state, we get

$$E_n(-i\vec{\nabla})\phi_{n\mathbf{k}}(\mathbf{r}) = \sum_{\mathbf{R}_l} E_{nl}\phi_{n\mathbf{k}}(\mathbf{r}+\mathbf{R}_l)$$
$$= \sum_{\mathbf{R}_l} E_{nl}e^{i\mathbf{k}\cdot\mathbf{R}_l}e^{i\mathbf{k}\cdot\mathbf{r}}u_{n\mathbf{k}}(\mathbf{r}) = E_n(\mathbf{k})\phi_{n\mathbf{k}}(\mathbf{r}). \tag{2.10}$$

Substituting Eqs.(2.3) and (2.10) into Eq. (2.6), we get

$$H_0\psi(\mathbf{r}) \approx \phi_{n0}(\mathbf{r})E_n(-i\vec{\nabla})\int \frac{\mathrm{d}(\mathbf{k})}{2\pi}A(\mathbf{k})e^{i\mathbf{k}\cdot\mathbf{r}} = \phi_{n0}(\mathbf{r})E_n(-i\vec{\nabla})F(\mathbf{r}), \tag{2.11}$$

where $F(\mathbf{r})$ is called as the envelope function [cf. Eq. (2.4)]. Now, instead of the periodic potential Hamiltonian, if we use another potential $[H_0+V(\mathbf{r})]$, the Schrödinger equation for wavepacket becomes

$$[H_0 + V(\mathbf{r})]\psi(\mathbf{r}) = E\psi(\mathbf{r}). \tag{2.12}$$

Substituting Eqs.(2.4) and (2.11) into Eq. (2.12) yields

$$\phi_{n0}(\mathbf{r})E_n(-i\vec{\nabla})F(\mathbf{r}) + V(\mathbf{r})\phi_{n0}(\mathbf{r})F(\mathbf{r}) = E\phi_{n0}(\mathbf{r})F(\mathbf{r}). \tag{2.13}$$

Then we obtain

$$[E_n(-i\vec{\nabla}) + V(\mathbf{r})]F(\mathbf{r}) = E\ F(\mathbf{r}), \tag{2.14}$$

where the Bloch functions do not appear at all. Eq. (2.14) is called the Luttinger equation [25]. Furthermore, we assume that the energy band structure $E(\mathbf{k})$ of the semiconductor is known either from the results of a theoretical calculation or from the analysis of experimental results. Thus we can write the energy around the point $\mathbf{k}_0 = 0$ in terms of the effective mass m^*. Let us assume that the conduction band (CB) of the semiconductor in the vicinity of the band "minimun" at $\mathbf{k}_0 = 0$ has the simple analytic form

$$E(\mathbf{k}) \approx \frac{\hbar^2\mathbf{k}^2}{2m^*}. \tag{2.15}$$

For the present discussion, the $E(\mathbf{k})$ is assumed to be isotropic in $\mathbf{k}$; this typically occurs in cubic semiconductors with the band extrema at $\mathbf{k}_0 = 0$. The operator $E_n(-i\vec{\nabla})$ thus becomes

$$E(-i\vec{\nabla}) \approx -\frac{\hbar^2}{2m^*}\nabla^2. \tag{2.16}$$

Substituting Eq.(2.16) into Eq. (2.14), the Schrödinger equation takes the simplified form

$$\left[\frac{\hbar^2}{2m^*}\nabla^2 + V(\mathbf{r})\right]F(\mathbf{r}) = E\ F(\mathbf{r}), \tag{2.17}$$

Eq. (2.17) is called the *effective mass equation*. The Schrödinger equation has been re-cast into a much simpler problem of a particle of effective mass m^* moving in a

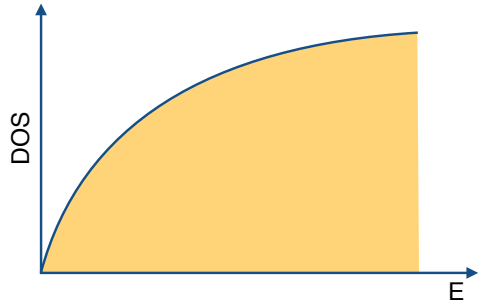

Figure 2.1: Density of states of bulk semiconductors.

potential $V(\mathbf{r})$. The effective mass m^* contains the information about the energy band structure and the crystal potential. In practical, the solution to the effective mass equation is much easier to carry out than the solution to the original Schrödinger equation.

2.1.2 Three-dimensional semiconductors

A three-dimensional (3D) semiconductor (or bulk semiconductor) in the absence of crystal fields, $V(\mathbf{r}) = 0$, and thus the solution of the effective mass equation [Eq. (2.17)] yields the envelope function as

$$F(\mathbf{r}) = \frac{1}{\sqrt{V}} e^{i\mathbf{k}\cdot\mathbf{r}}, \tag{2.18}$$

where $V = L_x L_y L_z$ is the crystal volume, and $E(\mathbf{k})$ given by

$$E(\mathbf{k}) = \frac{\hbar^2}{2}\left(\frac{k_x^2}{m_{xx}^*} + \frac{k_y^2}{m_{yy}^*} + \frac{k_z^2}{m_{zz}^*}\right), \tag{2.19}$$

where $k_x = n2\pi/L_x$, $k_y = n2\pi/L_y$, $k_z = n2\pi/L_z$ ($n = 0, \pm1, \pm2, \ldots$). Since L_x, L_y, and L_z are a macroscopic length in the 3D system, the quantization is almost continues. Hereafter, k_x, k_y and k_z can be assumed continuous.

For an isotropic system, $m_{xx}^* = m_{yy}^* = m_{zz}^* = m^*$, Eq. (2.19) thus becomes

$$E(\mathbf{k}) = \frac{\hbar^2\mathbf{k}^2}{2m^*}. \tag{2.20}$$

The volume of single quantum mechanical state in the 3D $\mathbf{k}$-space is $(2\pi)^3/L_xL_yL_z = 8\pi^3/V$. Thus the number of filled states in a sphere in the 3D $\mathbf{k}$-space is

$$N(\mathbf{k}) = 2\frac{\frac{4}{3}\pi\mathbf{k}^3}{8\pi^3/V} = \frac{V\mathbf{k}^3}{3\pi^2} \tag{2.21}$$

Fig. 2.1: Fig/chapter2-fig1.pdf

where the factor of two accounts for the freedom of spin. The density per unit energy is then obtained as

$$\frac{\mathrm{d}N}{\mathrm{d}E} = \left(\frac{\mathrm{d}N}{\mathrm{d}\mathbf{k}}\right)\left(\frac{\mathrm{d}\mathbf{k}}{\mathrm{d}E}\right) = \left(\frac{3V\mathbf{k}^2}{3\pi^2}\right)\left(\frac{2m^*}{2\hbar^2\mathbf{k}}\right) = \frac{V}{2\pi^2}\left(\frac{2m^*}{\hbar^2}\right)\mathbf{k} \tag{2.22}$$

Since $\mathbf{k} = (2m^*E/\hbar^2)^{1/2}$ from Eq. (2.20), the density of state (DOS) per unit volume and per unit energy [in unit of $\mathrm{m}^{-3}\mathrm{J}^{-1}$] for the 3D semiconductor is given by

$$g_{3\mathrm{D}}(E) = \frac{1}{V}\frac{\mathrm{d}N}{\mathrm{d}E} = \frac{1}{2\pi^2}\left(\frac{2m^*}{\hbar^2}\right)^{3/2} E^{1/2}. \tag{2.23}$$

DOS of the 3D system is shown in Fig. 2.1.

For a anisotropic system in the case of a multi-ellipsoidal energy surfaces, we introduce a new wavectors $\mathbf{k}'$ as a new effective mass m' as

$$k_x = \left(\frac{m^*_{xx}}{m'}\right)^{1/2} k'_x, \quad k_y = \left(\frac{m^*_{yy}}{m'}\right)^{1/2} k'_y, \quad k_z = \left(\frac{m^*_{zz}}{m'}\right)^{1/2} k'_z. \tag{2.24}$$

Then Eqs. (2.20) and (2.21) become as

$$E = \frac{\hbar^2 \mathbf{k}'^2}{2m'}, \tag{2.25}$$

and

$$N = \frac{V\mathbf{k}^3}{3\pi^2} = \left(\frac{m^*_{xx}m^*_{yy}m^*_{zz}}{m'^3}\right)^{1/2} \frac{V\mathbf{k}'^3}{3\pi^2} \tag{2.26}$$

From Eqs. (2.22) and (2.23), m' is eliminated, and DOS for the 3D anisotropic system is

$$g_{3\mathrm{D}}(E) = \frac{1}{V}\frac{\mathrm{d}N}{\mathrm{d}E} = \frac{1}{2\pi^2}\left(\frac{2m^*_d}{\hbar^2}\right)^{3/2} E^{1/2}, \tag{2.27}$$

where $m^*_d = (m^*_{xx}m^*_{yy}m^*_{zz})^{1/3}$, which is called the effective mass for density of states. Most energy band structures for the 3D semiconductors have ellipsoidal energy surfaces including longitudinal m^*_l and transverse effective masses m^*_t. Therefore, the density of states effective mass is $m^*_d = (m^*_l m^{*2}_t)^{1/3}$.

2.1.3 Two-dimensional semiconductors

A two-dimensional (2D) semiconductor (or quantum well) is formed upon sandwiching a thin film of semiconductor between two other materials, or a ultrathin semiconductor in a vacuum. For example, a thin film of GaAs (typically < 20 nm) can be sandwiched between two $\mathrm{Al}_x\mathrm{Ga}_{1-x}\mathrm{As}$ layers, as shown in Fig 2.2 (a). As sandwich structure, a potential difference exists at the interface in the both of the conduction band and valence band, called the band-edge offset. For electrons in the conduction band, the

Fig. 2.2: Fig/chapter2-fig2.pdf

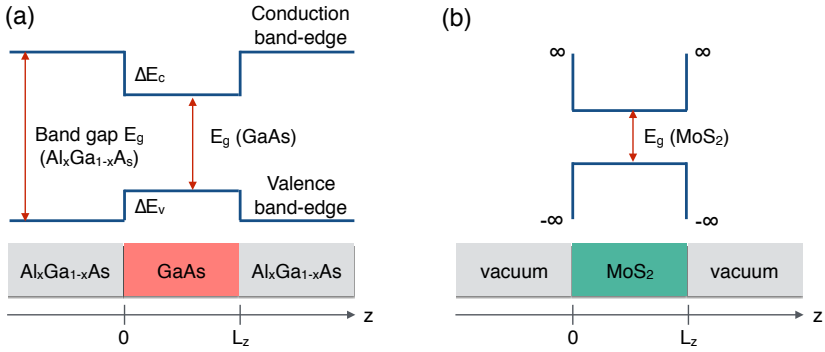

Figure 2.2: (a) A quantum well can be formed by sandwiching one material (GaAl) between two material ($Al_xGa_{1-x}As$). (b) A quantum well can be formed by ultrathin material (MoS_2) in the vacuum.

band-edge offset of the conduction band, ΔE_c, provides a potential barrier to from a quantum well. Similarly, the band-edge offset of the valence band, ΔE_v, provides a potential well for holes. A atomic layer material such as MoS_2 in a vacuum can be modeled as an infinitely deep potential well, as shown in Fig. 2.2 (b). We assume that the lengths (L_x, L_y) of the thin film are macroscopic length in the xy plane, and the thickness (L_z) is quantum confined in the z direction $(L_z \ll L_x, L_y)$. The potential well (with reference to the conduction band-edge E_{c0}) is written as

$$V(x,y,z) = \begin{cases} 0 & \text{if } z < 0 \\ 0 & \text{if } z > L_z \\ -\Delta E_c & \text{if } 0 \le z \le L_z \end{cases} \tag{2.28}$$

for model in Fig. 2.2 (a), or

$$V(x,y,z) = \begin{cases} 0 & \text{if } z < 0 \\ 0 & \text{if } z > L_z \\ \infty & \text{if } 0 \le z \le L_z \end{cases} \tag{2.29}$$

for model in Fig. 2.2 (b).

Using the effective mass equation in Eq. (2.17) with this potential, we obtain the envelope function as

$$F_{n_z}(x,y,z) = \phi(x,y)\chi_{n_z}(z) = \left(\frac{1}{\sqrt{A}} e^{i(k_x x + k_y y)}\right) \cdot \chi_{n_z}(z), \tag{2.30}$$

where $n_z = 1,\ 2,\ 3, \ldots$ is the quantum number, and $A = L_x L_y$ is the area along the xy plane. If the quantum well is assumed to be infinitely deep [e.g. Fig. 2.2(b)], the z component of the electron quasi-momentum is quantized to

$$k_{n_z} = \frac{2\pi}{\lambda} = \frac{\pi}{L_z} n_z, \tag{2.31}$$

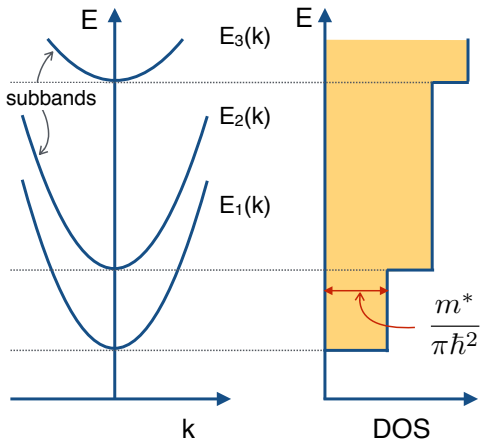

Figure 2.3: Energy band structure and DOS of a two-dimensional quantum well.

where λ is wavelength of the waves that satisfy $n_z(\lambda/2) = L_z$. From simple particle in a box model in quantum mechanics, the normalized z component of the envelope function is

$$\chi_{n_z}(z) = \sqrt{\frac{2}{L_z}} \sin \frac{\pi n_z}{L_z} z. \tag{2.32}$$

The energy band structure which is the set of energy eigenvalues is obtained from the effective mass equation, given by

$$E(k_x, k_y, n_z) = \frac{\hbar^2}{2} \left(\frac{k_x^2}{m_{xx}^*} + \frac{k_y^2}{m_{yy}^*} \right) + \frac{\hbar^2}{m_{zz}^*} \left(\frac{\pi n_z}{L_z} \right)^2, \tag{2.33}$$

which is separated into a free-electron component in the xy plane and a quantized component in the z direction. Therefore, the energy band structure of the 2D system including multiple energy subbands. Each subband is indexed by the quantum number $n_z = 1,\ 2,\ 3, \ldots$, as shown in Fig 2.3.

For an isotropic system, $m_{xx}^* = m_{yy}^* = m_{zz}^* = m^*$, Eq. (2.33) thus becomes

$$E(k_{xy}, n_z) = \frac{\hbar^2 k_{xy}}{2m^*} + \frac{\hbar^2}{m^*} \left(\frac{\pi n_z}{L_z} \right)^2, \tag{2.34}$$

where $k_{xy}^2 = k_x^2 + k_y^2$. The area of each quantum mechanical state in the 2D $\mathbf{k}$-space is $(2\pi)^2/L_x L_y = 4\pi^2/A$. Thus, the number of states in a circle for each of n_z values is

$$N(k_{xy}) = 2\frac{\pi k_{xy}^2}{4\pi^2/A} = \frac{A k_{xy}}{2\pi} \tag{2.35}$$

Fig. 2.3: Fig/chapter2-fig3.pdf

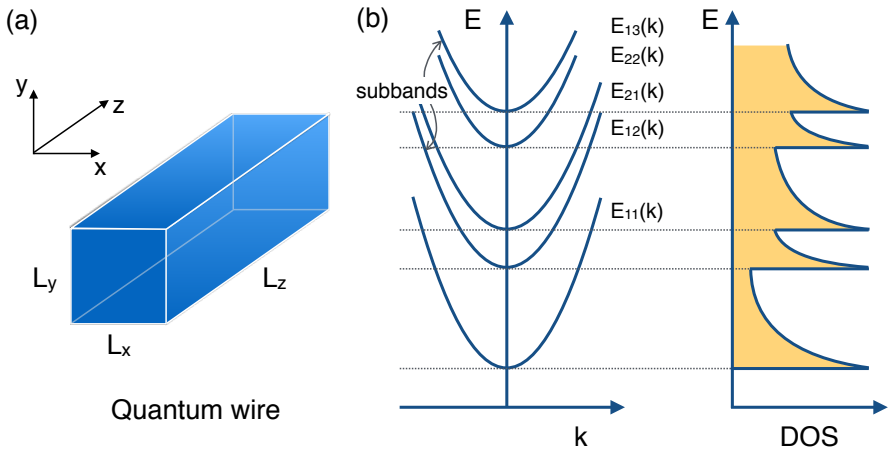

Figure 2.4: (a) Model of a one-dimensional quantum wire. (b) Energy band structure and DOS of the quantum wire.

where $k_{xy}^2 = k_x^2 + k_y^2$. Then the density of states (DOS) per unit area and per unit energy [in unit of $\mathrm{m}^{-2}\mathrm{J}^{-1}$] for the 2D semiconductor is given by

$$g_{2\mathrm{D}}(E) = \frac{1}{A}\frac{\mathrm{d}N}{\mathrm{d}E} = \frac{1}{A}\left(\frac{\mathrm{d}N}{\mathrm{d}k_{xy}}\right)\left(\frac{\mathrm{d}k_{xy}}{\mathrm{d}E}\right) = \frac{m^*}{\pi\hbar^2}. \tag{2.36}$$

In the quantum well, each subband labeled by n_z is an ideal 2D system, and each subband contributes to the total DOS, as shown in Fig 2.3. Thus, the DOS of the quantum well is

$$g_{\mathrm{QWell}}(E) = \frac{m^*}{\pi\hbar^2}\sum_{n_z}\theta(E - E_{n_z}), \tag{2.37}$$

where $\theta(x)$ is the step function, and $E_{n_z} = (\hbar^2/m^*)(\pi n_z/L_z)^2$ [cf. Eq. (2.34)].

For a anisotropic system, then similar to the 3D system situation, the DOS of the 2D system gives

$$g_{2\mathrm{D}}(E) = \frac{(m_{xx}^* m_{yy}^*)^{1/2}}{\pi\hbar^2}, \tag{2.38}$$

which depends on the effective masses m_{xx}^* and m_{yy}^* of the xy plane.

2.1.4 One-dimensional semiconductors

A one-dimensional (1D) semiconductor (or quantum wire) is formed either lithographically (top-down approach), or by direct growth in the form of semiconducting nanowires or nanotubes (bottom-up approach). In a quantum well, the carriers (electrons or holes) are confined in one direction, and they are free to move in two other directions. While, in a quantum wire, the carriers are free to move freely in

Fig. 2.4: Fig/chapter2-fig4.pdf

one direction only, and two other directions are confined. We assume that the 1D system has a length (L_z) along the z direction, and the system is confined in the xy plane ($L_x, L_y \ll L_z$), as shown in Fig 2.4 (a). Then, the solution of the effective mass equation in Eq. (2.17) yields the envelope function

$$F_{n_x,n_y}(x,y,z) = \chi_{n_x}(x) \cdot \chi_{n_y}(y) \cdot \left(\frac{1}{\sqrt{L_z}} e^{ik_z z} \right), \tag{2.39}$$

where $n_x, n_y = 1,\ 2,\ 3, \ldots$ are the quantum numbers, and the energy eigenvalues are given by

$$E(n_x, n_y, k_z) = E(n_x, n_y) + \frac{\hbar^2 k_z^2}{2m^*_{zz}}. \tag{2.40}$$

If the confinement in the xy plane is expressed by an infinite potential, the electron quasi-momentums are quantized to

$$k_{n_x} = \frac{\pi}{L_x} n_x, \quad k_{n_y} = \frac{\pi}{L_y} n_y, \tag{2.41}$$

where $n_x, n_y = 1,\ 2,\ 3, \ldots$. The envelope function in Eq. (2.39) can be rewritten as

$$F_{n_x,n_y}(x,y,z) = \left(\sqrt{\frac{2}{L_x}} \sin \frac{\pi n_x}{L_x} x \right) \cdot \left(\sqrt{\frac{2}{L_y}} \sin \frac{\pi n_y}{L_y} y \right) \cdot \left(\frac{1}{\sqrt{L_z}} e^{ik_z z} \right), \tag{2.42}$$

and Eq. (2.40) is explicitly given by

$$E(n_x, n_y, k_z) = \frac{\hbar^2}{2m^*_{xx}} \left(\frac{\pi n_x}{L_x} \right)^2 + \frac{\hbar^2}{2m^*_{yy}} \left(\frac{\pi n_y}{L_y} \right)^2 + \frac{\hbar^2 k_z^2}{2m^*_{zz}}. \tag{2.43}$$

Energy band structure including multiple subbands is thus formed. For each eigenvalue $E(n_x, n_y)$ with the quantum numbers $n_x, n_y = 1,\ 2,\ 3, \ldots$, the subband has a dispersion as a function of k_z,

$$E(k_z) = \frac{\hbar^2 k_z^2}{2m^*_{zz}}, \tag{2.44}$$

and the number of states in the wire is given by

$$N(k_z) = 2\frac{2k_z}{2\pi/L_z} = \frac{2L_z k_z}{\pi}. \tag{2.45}$$

Then for each pair of n_x, n_y values, the density of states (DOS) per unit length and per unit energy [in unit of $\mathrm{m}^{-1}\mathrm{J}^{-1}$] for the 1D system is given by

$$g_{1\mathrm{D}}(E) = \frac{1}{L_z}\frac{\mathrm{d}N}{\mathrm{d}E} = \frac{1}{L_z}\left(\frac{\mathrm{d}N}{\mathrm{d}k_z}\right)\left(\frac{\mathrm{d}k_z}{\mathrm{d}E}\right) = \frac{1}{\pi}\left(\frac{2m^*_{zz}}{\hbar^2}\right)^{1/2} E^{-1/2}. \tag{2.46}$$

Due to multiple subbands, the 1D van Hove singularity of the DOS peaks appear at every eigenvalue $E(n_x, n_y)$. Since there are two quantum numbers involved (n_x, n_y),

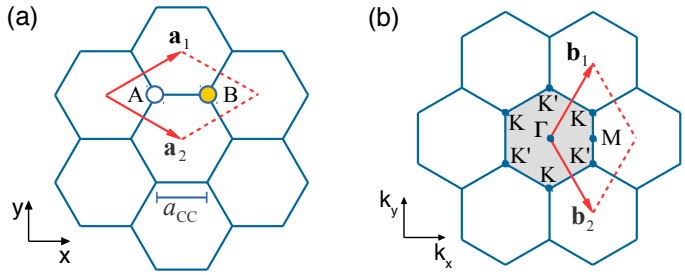

Figure 2.5: (a) The unit cell of graphene in real space contains two carbon atoms A and B, and two lattice vectors $\mathbf{a}_1$ and $\mathbf{a}_2$. (b) The Brillouin zone of graphene contains two reciprocal lattice vectors $\mathbf{b}_1$ and $\mathbf{b}_2$, and the high-symmetry points K, K′, M and Γ.

some eigenvalues can be degenerate. Thus, the peak height and position appear at irregular intervals. The DOS for the quantum wire can be written as

$$g_{\mathrm{QWire}}(E) = \frac{1}{\pi}\left(\frac{2m^*_{zz}}{\hbar^2}\right)^{1/2} \sum_{n_x,n_y} \big(E - E(n_x,n_y)\big)^{-1/2}, \tag{2.47}$$

which is shown in Fig 2.4 (b).

2.2 Graphene and carbon nanotube

2.2.1 Graphene unit cell

Graphene is a single atomic layer of carbon atoms in a two-dimensional (2D) honeycomb lattice. The graphene sheet is generated from the dotted rhombus unit cell generated by the lattice vectors $\mathbf{a}_1$ and $\mathbf{a}_2$, which are defined in (x, y) coordinate as

$$\mathbf{a}_1 = a\left(\frac{\sqrt{3}}{2}, \frac{1}{2}\right), \quad \mathbf{a}_2 = a\left(\frac{\sqrt{3}}{2}, -\frac{1}{2}\right), \tag{2.48}$$

where $a = \sqrt{3}a_{CC}$ is the lattice constant for the graphene, and $a_{CC} \approx 0.142$ nm is the nearest-neighbor carbon-carbon atom distance. Figure 2.5 (a) shows the unit cell that contains two carbon atoms A and B by open and solid dots, respectively.

The reciprocal lattice vectors $\mathbf{b}_1$ and $\mathbf{b}_2$ are related to the real lattice vectors $\mathbf{a}_1$ and $\mathbf{a}_2$ according to the definition

$$\mathbf{a}_i \cdot \mathbf{b}_j = 2\pi\delta_{ij}, \tag{2.49}$$

where δ_{ij} is the Kronecker delta. From Eqs. (2.48) and (2.49), $\mathbf{b}_1$ and $\mathbf{b}_2$ are given by

$$\mathbf{b}_1 = \frac{2\pi}{a}\left(\frac{1}{\sqrt{3}}, 1\right), \quad \mathbf{b}_2 = \frac{2\pi}{a}\left(\frac{1}{\sqrt{3}}, -1\right). \tag{2.50}$$

Figure 2.5 (b) shows the first Brillouin zone as a shaded hexagon, where Γ (center), K, K′ (hexagonal corners), and M (center of edges) denote the high symmetry points.

Fig. 2.5: Fig/chapter2-fig5.pdf

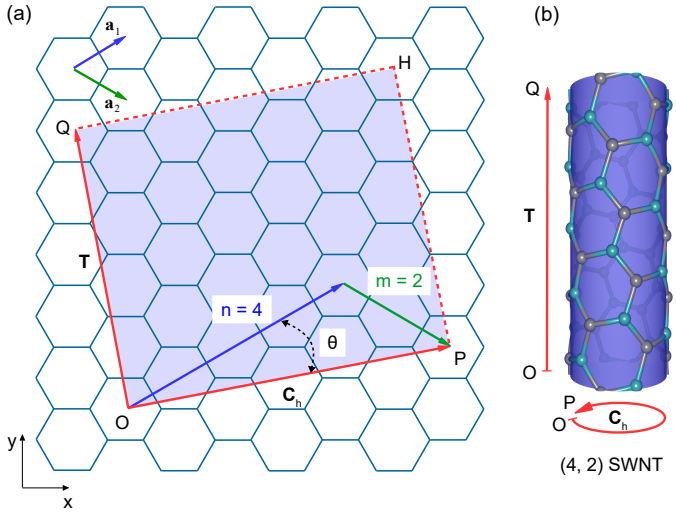

Figure 2.6: (a) Geometry of a (4, 2) SWNT viewed as an unrolled graphene sheet with the graphene unit vectors $\mathbf{a}_1$ and $\mathbf{a}_2$. The shaded rectangle OPHQ is a one-dimensional unit cell of the (4, 2) SWNT. OP and OQ define the chiral vector $\mathbf{C}_h = (4, 2)$ and the translational vector $\mathbf{T} = (4, -5)$, respectively. The chiral angle θ is the angle between $\mathbf{a}_1$ and $\mathbf{C}_h$. (b) Perspective view of the (4, 2) SWNT in three dimensional space.

2.2.2 Carbon nanotube unit cell

Carbon nanotube is one-dimensional (1D) cylindrical structure made of carbon, which is non-Bravais lattice. A single wall carbon nanotube (SWNT) can be thought of as a sheet of graphene rolled into a cylinder. As shown in Fig. 2.6 (a), the unit cell of a SWNT is expressed by the two vectors including the chiral vector $\mathbf{C}_h$ and the translational vector $\mathbf{T}$. $\mathbf{C}_h$ is defined as the circumference of a SWNT, while the $\mathbf{T}$ is determined by a vector perpendicular to $\mathbf{C}_h$ in the direction of the nanotube axis.

The chiral vector $\mathbf{C}_h$ can be written in terms of the unit vectors of graphene $\mathbf{a}_1$ and $\mathbf{a}_2$,

$$\mathbf{C}_h = n\mathbf{a}_1 + m\mathbf{a}_2 \equiv (n, m), \tag{2.51}$$

where (n, m) is a pair of integer indices with $0 \leq |m| \leq n$. Since $\mathbf{C}_h$ determines the circumference of the SWNT, it is straightforward to obtain the relations for the circumferential length L and the diameter d_t as

$$\begin{aligned} L &= |\mathbf{C}_h| = a\sqrt{n^2 + nm + m^2}, \\ d_t &= \frac{L}{\pi} = \frac{a\sqrt{n^2 + nm + m^2}}{\pi}. \end{aligned} \tag{2.52}$$

The chiral angle θ is the angle between $\mathbf{C}_h$ and $\mathbf{a}_1$, with values of θ in the range of $0 \leq |\theta| \leq 30°$. $\cos\theta$ can be obtained by taking the inner product of $\mathbf{C}_h$ and $\mathbf{a}_1$, thus

Fig. 2.6: Fig/chapter2-fig6.pdf

relating θ to the chiral index (n, m) can be expressed as

$$\cos\theta = \frac{\mathbf{C}_h \cdot \mathbf{a}_1}{|\mathbf{C}_h||\mathbf{a}_1|} = \frac{2n+m}{2\sqrt{n^2+nm+m^2}}. \tag{2.53}$$

The translation vector $\mathbf{T}$, then similar to $\mathbf{C}_h$, can be written in terms of $\mathbf{a}_1$ and $\mathbf{a}_2$,

$$\mathbf{T} = t_1\mathbf{a}_1 + t_2\mathbf{a}_2 \equiv (t_1, t_2), \tag{2.54}$$

where t_1 and t_2 are integers, and its are obtained from the condition $\mathbf{C}_h \cdot \mathbf{T} = 0$ because $\mathbf{T}$ is perpendicular to $\mathbf{C}_h$

$$t_1 = \frac{2m+n}{d_R}, \quad t_2 = -\frac{2n+m}{d_R}, \tag{2.55}$$

where d_R is the greatest common divisor of $(2m+n)$ and $(2n+m)$. The length of the translation vector, T, is then given by

$$T = |\mathbf{T}| = \sqrt{3}\frac{L}{d_R}. \tag{2.56}$$

The area of SWNT unit cell is defined as the rectangular area determined by two vector $\mathbf{C}_h$ and $\mathbf{T}$. This area is given by the magnitude of the vector product of $\mathbf{C}_h$ and $\mathbf{T}$. Since the area of the hexagonal unit cell in the graphene is $|\mathbf{a}_1 \times \mathbf{a}_2|$, the number of hexagons per SWNT unit cell, N, is obtained by

$$N = \frac{|\mathbf{C}_h \times \mathbf{T}|}{|\mathbf{a}_1 \times \mathbf{a}_2|} = \frac{2(n^2+nm+m^2)}{d_R}. \tag{2.57}$$

We note that each hexagon contains two carbon atoms [Fig. 2.5 (a)]. Thus there are $2N$ carbon atoms in each SWNT unit cell. The geometry of the SWNT is shown in Fig. 2.6 (b). The SWNT can then be classified according to its (n, m) or θ values. This classification is based on the symmetry of the SWNT. There are three types of SWNT: (a) zigzag nanotube corresponds the the case of $m = 0$ or $\theta = 0°$, (b) armchair nanotube corresponds to the case of $n = m$ or $\theta = 30°$, (c) all other (n, m) or θ correspond to chiral nanotubes. We note that the hexagonal symmetry of the honeycomb lattice, we thus need to consider only $0 \leq |m| \leq n$ or $0 \leq \theta \leq 30°$ for chiral nanotubes.

Since the 1D unit cell of a SWNT in real space is expressed by two vector $\mathbf{C}_h$ and $\mathbf{T}$ [Fig. 2.6 (b)], the corresponding vectors in reciprocal space are the vectors $\mathbf{K}_1$ along the tube circumference and $\mathbf{K}_2$ along the tube axis. Expressions for $\mathbf{K}_1$ and $\mathbf{K}_2$ are obtained from their relations with $\mathbf{C}_h$ and $\mathbf{T}$ as

$$\begin{aligned} &\mathbf{C}_h \cdot \mathbf{K}_1 = 2\pi, \quad \mathbf{T} \cdot \mathbf{K}_1 = 0, \\ &\mathbf{C}_h \cdot \mathbf{K}_2 = 0, \quad\quad \mathbf{T} \cdot \mathbf{K}_2 = 2\pi. \end{aligned} \tag{2.58}$$

Fig. 2.7: Fig/chapter2-fig7.pdf

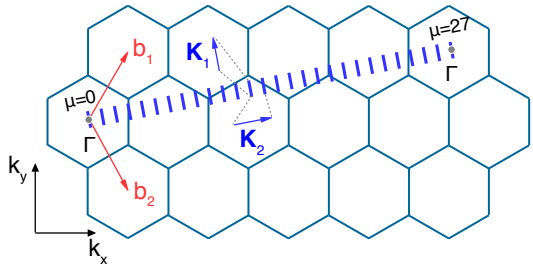

Figure 2.7: Reciprocal space of the graphene sheet with reciprocal lattice unit vectors $\mathbf{b}_1$ and $\mathbf{b}_2$. Parallel equidistant lines represent the cutting lines for the (4, 2) SWNT labeled by the cutting line index μ from 0 to 27. The vectors $\mathbf{K}_1$ and $\mathbf{K}_2$ in reciprocal space correspond to $\mathbf{C}_h$ and $\mathbf{T}$ in real space, respectively.

It follows,

$$\mathbf{K}_1 = \frac{1}{N}(-t_2\mathbf{b}_1 + t_1\mathbf{b}_2), \quad \mathbf{K}_2 = \frac{1}{N}(m\mathbf{b}_1 - n\mathbf{b}_2), \tag{2.59}$$

where $\mathbf{b}_1$ and $\mathbf{b}_2$ are the reciprocal lattice vector of graphene. The N line segments with length of $\mathbf{K}_2$ and the separation of $\mathbf{K}_1$ construct the 1D Brillouin zone of the SWNT shown in 2D $\mathbf{k}$-space of graphene, which we call as "cutting lines" [12], as shown in Fig. 2.7. The allowed wavevector $\mathbf{k}$ of a SWNT is

$$\mathbf{k} = \mu\mathbf{K}_1 + k\frac{\mathbf{K}_2}{|\mathbf{K}_2|}, \tag{2.60}$$

where $\mu = 0,\ 1, \ldots,\ N-1$ is the "cutting lines" index, and k is the range of $-\pi/T < k < \pi/T$ ($T = |\mathbf{T}|$ is length of the translation vector). The length of $\mathbf{K}_1$ and $\mathbf{K}_2$ are given by

$$|\mathbf{K}_1| = \frac{2\pi}{L} = \frac{2}{d_t}, \quad |\mathbf{K}_2| = \frac{2\pi}{T}. \tag{2.61}$$

For example, the unit cell of the (4, 2) SWNT contains $N = 28$ hexagons. Therefore, the first Brillouin zone of the (4, 2) SWNT consists of 28 cutting lines labeled by the cutting line index μ from 0 to 27, as shown in Fig. 2.7.

2.2.3 Electronic properties of SWNTs

The electronic energy dispersion relations of SWNTs are derived from those of a graphene sheet. The tight-binding model is reviewed here, starting from a simple tight-binding (STB) model. In a later section, we further develop an extended tight-binding (ETB) model that gives a good agreement with some optical spectroscopy measurements as well as with first principles density function theory calculations.

The electronic energy dispersion relations of graphene are obtained by solving the single particle Schrödinger equation

$$H\Psi^b(\mathbf{k}, \mathbf{r}, t) = i\hbar\frac{\partial}{\partial t}\Psi^b(\mathbf{k}, \mathbf{r}), \tag{2.62}$$

where $H = T + V(\mathbf{r})$ is single-particle Hamiltonian, $T = \mathbf{p}^2/2m$ is the kinetic energy operator, $\mathbf{p} = -i\hbar\nabla$, ∇ is the gradient operator, $\hbar$ is Planck's constant, m is the electron mass, $V(\mathbf{r})$ is the periodic potential, $\Psi^b(\mathbf{k}, \mathbf{r}, t)$ is the one-electron wavefunction, where b is the band index, $\mathbf{k}$ is the electron wavevector, $\mathbf{r}$ is the spatial coordinate, t is time, and i is imaginary unity. The electron wavefunction $\Psi^b(\mathbf{k}, \mathbf{r}, t)$ is approximated by a linear combination of atomic orbitals (LCAO) in terms of Bloch functions as

$$\begin{cases} \Psi^b(\mathbf{k}, \mathbf{r}, t) = \exp\big(-iE^b(\mathbf{k})t/\hbar\big) \sum\limits_{so} C^b_{so}(\mathbf{k})\Phi(\mathbf{k}, \mathbf{r}) \\ \Phi(\mathbf{k}, \mathbf{r}) = \frac{1}{\sqrt{N_u}} \sum\limits_{u}^{N_u} \exp(i\mathbf{k}\mathbf{R}_{us})\Phi(\mathbf{k}, \mathbf{r}) \end{cases}, \tag{2.63}$$

where $E^b(\mathbf{k}$ is the one-electron energy, $C^b_{so}(\mathbf{k})$ is the Bloch amplitude, $\Phi(\mathbf{k}, \mathbf{r})$ is the Bloch wavefunction, $\Phi(\mathbf{k}, \mathbf{r})$ is the atomic orbital, $\mathbf{R}_{us}$ is the atomic coordinate, the index $u = 1,\ 2, \ldots,\ N_u$ spans all the N_u unit cells in a graphene sheet ($N_u = N$ for a SWNT), the index $s = A,\ B$ labels the tow inequivalent atoms in the unit cell, and the index $o = 1s,\ 2s,\ 2p_x,\ 2p_y,\ 2p_z$ enumerates the atomic orbitals of a carbon atom.

The Schrödinger equation for the Bloch amplitudes $C^b_{so}(\mathbf{k})$ can be written in the matrix form

$$\sum_{so} H_{s'o'so}(\mathbf{k})C^b_{so}(\mathbf{k}) = \sum_{so} E^b(\mathbf{k})S_{s'o'so}(\mathbf{k})C^b_{so}(\mathbf{k}), \tag{2.64}$$

where the Hamiltonian $H_{s'o'so}(\mathbf{k})$ and overlap $S_{s'o'so}(\mathbf{k})$ matrices are given by

$$\begin{cases} H_{s'o'so}(\mathbf{k}) = \sum\limits_{uu'ss'}^{N_u} \exp\big(i\mathbf{k}(\mathbf{R}_{us} - \mathbf{R}_{u's'})\big) \int \phi^*_{o'}(\mathbf{r} - \mathbf{R}_{u's'})H\phi_o(\mathbf{r} - \mathbf{R}_{us})\mathrm{d}\mathbf{r} \\ S_{s'o'so}(\mathbf{k}) = \sum\limits_{uu'ss'}^{N_u} \exp\big(i\mathbf{k}(\mathbf{R}_{us} - \mathbf{R}_{u's'})\big) \int \phi^*_{o'}(\mathbf{r} - \mathbf{R}_{u's'})\phi_o(\mathbf{r} - \mathbf{R}_{us})\mathrm{d}\mathbf{r} \end{cases}, \tag{2.65}$$

and the index u' labels the unit cell under consideration. The orthonormality condition for the electron wavefuction of Eq. (2.63) becomes

$$\int \Psi^{b'^*}(\mathbf{k}, \mathbf{r}, t)\Psi^{b'}(\mathbf{k}, \mathbf{r}, t)\mathrm{d}\mathbf{r} = \sum_{s'o'} \sum_{so} C^{b'^*}_{s'o'}(\mathbf{k})S_{s'o'so}(\mathbf{k})C^b_{so}(\mathbf{k}) = \delta_{b'b}, \tag{2.66}$$

where $\delta_{b'b}$ is the Kronecher delta function. To evaluate the integrals in Eq. (2.65), the effective periodic potential $V(\mathbf{k})$ in the single-particle Hamiltonian H of Eq. (2.62) is expressed by a sum of the effective spherically-symmetric potentials $U(\mathbf{r} - \mathbf{R}_{u''s''})$ centered at the atomic sites $\mathbf{R}_{u''s''}$

$$V(\mathbf{r}) = \sum_{u''s''} U(\mathbf{r} - \mathbf{R}_{u''s''}). \tag{2.67}$$

The Hamiltonian matrix $H_{s'o'so}(\mathbf{k})$ then contains the three-center integrals that involve two orbitals $\phi^*_{o'}(\mathbf{r} - \mathbf{R}_{u's'})$ and $\phi_{o'}(\mathbf{r} - \mathbf{R}_{us})$ at two different atomic sites $\mathbf{R}_{u's'}$ and

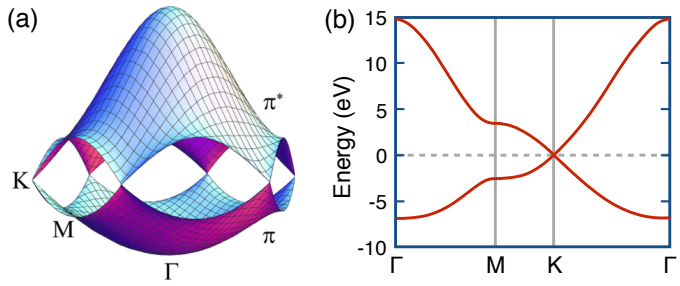

Figure 2.8: Electronic dispersion relations of a graphene given by Eq. (2.71) with STB parameters $t = -3.033$ eV, $s = 0.129$, and $\varepsilon = 0$ eV (a) throughout the entire first Brillouin zone shown in Fig. 2.5 (b) and (b) along the high-symmetry directions in the first Brillouin zone. The Fermi level is shown by the dotted line at zero energy.

$\mathbf{R}_{us}$, while the potential $U(\mathbf{r} - \mathbf{R}_{u''s''})$ originates from a third atomic site $R_{u''s''}$. On the other hand, the overlap matrix $S_{s'o'so}(\mathbf{k})$ contains two-center integrals only. Neglecting the three-center integrals in $H_{s'o'so}(\mathbf{k})$, the remaining two-center integrals in both $H_{s'o'so}(\mathbf{k})$ and $S_{s'o'so}(\mathbf{k})$ can be parameterized as functions of the interatomic vector $\mathbf{R} = \mathbf{R}_{us} - \mathbf{R}_{u's'}$. The symmetry and relative orientation of the atomic orbitals $\phi^*_{o'}(\mathbf{r})$ and $\phi_o(\mathbf{r})$ as follow

$$\begin{cases} \varepsilon_o = \int \phi^*_o(\mathbf{r}) H \phi_o(\mathbf{r}) \mathrm{d}\mathbf{r} \\ t_{o'o}(\mathbf{R}) = \int \phi^*_{o'}(\mathbf{r}) \big(T + U(\mathbf{r}) + U(\mathbf{r} - \mathbf{R})\big) \phi_o(\mathbf{r} - \mathbf{R}) \mathrm{d}\mathbf{r} \\ s_{o'o}(\mathbf{R}) = \int \phi^*_{o'}(\mathbf{r}) \phi_o(\mathbf{r} - \mathbf{R}) \mathrm{d}\mathbf{r} \end{cases} , \tag{2.68}$$

where ε_o is the energy of atomic orbital. The transfer $t_{o'o}(\mathbf{R})$ and the overlap $s_{o'o}(\mathbf{R})$ integrals depend on the relative orientation of the atomic orbitals o' and o with respect to the interatomic vector $\mathbf{R}$. A numerical calculation of parameters ε_o, $t_{o'o}(\mathbf{R})$, and $s_{o'o}(\mathbf{R})$ defines the non-orthogonal tight-binding model. Within the orthogonal tight-binding model, $s_{o'o}(\mathbf{R})$ is set to zero (unity) for $\mathbf{R} \neq 0$ ($\mathbf{R} = 0$).

2.2.4 Simple tight-binding model

Within the framework of the simple tight-binding (STB) model, we neglect the σ ($2s$, $2p_x$, $2p_y$) molecular orbitals and the long-range atomic interactions in the π ($2p_z$) molecular orbitals. The STB model thus has three parameters including the atomic orbital energy ε_{2p}, the transfer integral $t_{\pi\pi}(a_{\mathrm{CC}})$, and the overlap integral $s_{\pi\pi}(a_{\mathrm{CC}})$, where a_{CC} is the nearest-neighbor interatomic distance. Thereafter we refer to these parameters as ε, t, and s, respectively, for simplicity.

Fig. 2.8: Fig/chapter2-fig8.pdf

The unit cell contains two atoms, A and B, [Fig. 2.5 (a)] each of which has three nearest-neighbors ($R = a_{\mathrm{CC}}$) of the opposite atom type. The absence of nearest-neighbor interactions within the same A or B sublattice gives the diagonal Hamiltonian and overlap matrix elements, $H_{\mathrm{A}\pi\mathrm{A}\pi} = H_{\mathrm{B}\pi\mathrm{B}\pi} = \varepsilon_{2p}$ and $S_{\mathrm{A}\pi\mathrm{A}\pi} = S_{\mathrm{B}\pi\mathrm{B}\pi} = 1$ independent of the transfer t and overlap s integrals. For the $H_{\mathrm{A}\pi\mathrm{B}\pi}$ and $S_{\mathrm{A}\pi\mathrm{B}\pi}$ matrix elements, the interatomic vector $\mathbf{R}$ from atom A to its three nearest-neighbors are given by $(\mathbf{a}_1 + \mathbf{a}_2)/3$, $(\mathbf{a}_1 - 2\mathbf{a}_2)/3$, and $(\mathbf{a}_2 - 2\mathbf{a}_1)/3$, where $\mathbf{a}_1$ and $\mathbf{a}_2$ are the lattice vectors in Eq. (2.48). Substituting these vectors from Eq. (2.64), one can obtain $H_{\mathrm{A}\pi\mathrm{B}\pi} = tf(\mathbf{k})$ and $S_{\mathrm{A}\pi\mathrm{B}\pi} = sf(\mathbf{k})$, where $f(\mathbf{k})$ is sum of the phase factors over the nearest-neighbors given by

$$f(\mathbf{k}) = \exp\left(i\frac{k_x a}{\sqrt{3}}\right) + \exp\left(-i\frac{k_x a}{2\sqrt{3}} + i\frac{k_y a}{2}\right) + \exp\left(-i\frac{k_x a}{2\sqrt{3}} - i\frac{k_y a}{2}\right). \tag{2.69}$$

Since the interatomic vectors $\mathbf{R}$ have the opposite signs, $H_{\mathrm{B}\pi\mathrm{A}\pi} = tf^*(\mathbf{k})$ and $S_{\mathrm{B}\pi\mathrm{A}\pi} = sf^*(\mathbf{k})$. The Schrödinger equation Eq. (2.64) can be written as

$$\begin{pmatrix} \varepsilon_{2p} & tf(\mathbf{k}) \\ tf^*(\mathbf{k}) & \varepsilon_{2p} \end{pmatrix} \begin{pmatrix} C^b_{\mathrm{A}\pi}(\mathbf{k}) \\ C^b_{\mathrm{B}\pi}(\mathbf{k}) \end{pmatrix} = E^b(\mathbf{k}) \begin{pmatrix} 1 & sf(\mathbf{k}) \\ sf^*(\mathbf{k}) & 1 \end{pmatrix} \begin{pmatrix} C^b_{\mathrm{A}\pi}(\mathbf{k}) \\ C^b_{\mathrm{B}\pi}(\mathbf{k}) \end{pmatrix}. \tag{2.70}$$

Solving this secular equation yields the energy eigenvalues

$$E^v(\mathbf{k}) = \frac{\varepsilon + t\omega(\mathbf{k})}{1 + s\omega(\mathbf{k})}, \quad E^c(\mathbf{k}) = \frac{\varepsilon - t\omega(\mathbf{k})}{1 - s\omega(\mathbf{k})}, \tag{2.71}$$

where the band index $b = v,\ c$ indicates the valence and conduction bands, $t < 0$, and $\omega(\mathbf{k})$ is the absolute value of the phase factor $f(\mathbf{k})$, i.e.,

$$\omega(\mathbf{k}) = \sqrt{f^*(\mathbf{k}) f(\mathbf{k})} = \sqrt{1 + 4\cos\frac{\sqrt{3}k_x a}{2}\cos\frac{k_y a}{2} + 4\cos^2\frac{k_y a}{2}} \tag{2.72}$$

Fitting the dispersion relations of valence and conduction bands in Eq. (2.71) to the energy values obtained from an first-principles calculations for graphene [26] yields the values of the transfer $t = -3.033$ eV and overlap $s = 0.129$ integrals, after setting the atomic orbital energy equal to zero of the energy scale, $\varepsilon = 0$ eV. Figures 2.8 (a) and (b) show the dispersion relations of the graphene using the STB with the above parameters throughout the entire first Brillouin zone and along the high symmetry directions in the first Brillouin zone, respectively.

The band structure of a graphene in Fig. 2.8 (b) shows linear dispersion relations around K and K′ points near the Fermi level. The electron wavevector around the K point in the first Brillouin zone can be written in the form $k_x = \Delta k_x$ and $k_y = -4\pi/(3a) + \Delta k_x$, where Δk_x and Δk_y are small compared with 1/a. Substituting this wavevector into Eq. (2.72), we can obtain $\omega = \frac{\sqrt{3}}{2} a\Delta k$, where $\Delta k = \sqrt{\Delta k_x^2 + \Delta k_y^2}$ is the distance from the electron wavevector to the K point. Substituting ω into

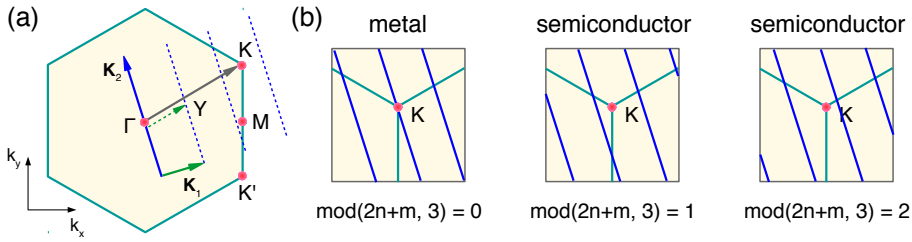

Figure 2.9: (a) Condition for metallic or semiconducting SWNT is related to the ratio of the length of vector **ΓK** to that of **ΓY**, if the ratio is an integer, metallic SWNT is obtained. (b) Three possible configurations of the cutting lines in the vicinity of the **K** point depending on the value of $\mod(2n+m, 3)$. From left to right, the nanotube type is M- (metallic), S1- (semiconducting), and S2- (semiconducting) SWNT, respectively.

Eq. (2.71) yields the electronic dispersion relations in the valence and conduction bands near K point as

$$E^v(\Delta k) = \varepsilon - \frac{\sqrt{3}}{2}(\varepsilon s - t)a\Delta k, \quad E^c(\Delta k) = \varepsilon + \frac{\sqrt{3}}{2}(\varepsilon s - t)a\Delta k, \tag{2.73}$$

which are linear in Δk. The linear dispersion relations near the Fermi level imply that the effective mass approximation used for semiconductors with parabolic energy bands is not applicable to a graphene. Instead, the π electrons in a graphene mimic massless particles whose behavior is described by the relativistic Dirac equation. Besides, the linear dispersion relations increase the mobility of the conducting π electrons in a graphene compared to conventional semiconductors [27].

Now the electronic structure of a SWNT can be derived from the energy dispersion calculation of graphene in Eq. (2.71). Since the allowed wavevectors $\mathbf{k}$ (the cutting lines) around the SWNT circumference become quantized, the energy dispersion relations (E^b_{SWNT}) of the SWNT are given by the corresponding energy dispersion relations (E^b_{2D}) of a graphene along the cutting lines. Using the cutting lines from Eq. (2.60), we can obtain the energy dispersion relations of the SWNT as

$$E^b_{\mathrm{SWNT}}(\mu, k) = E^b_{\mathrm{2D}}\left(\mu\mathbf{K}_1 + k\frac{\mathbf{K}_2}{|\mathbf{K}_2|}\right), \tag{2.74}$$

where $\mu = 0,\ 1, \ldots,\ N-1$ and $-\pi/T < k < \pi/T$. For a particular $(n,\ m)$ SWNT, if a cutting line passes through K or K′ points of the Brillouin zone of graphene, where the valence and conduction bands touch to each other, the band structure of the SWNT have a zero band gap, they thus become metal. However, if a cutting line does not pass through K or K′ points, the band structure of the SWNT have a finite band gap, they thus become semiconductor.

As shown in Fig. 2.9 (a), SWNT can be either metallic or semiconducting, depending on whether one of the cutting lines crosses the K point or not, respectively.

Fig. 2.9: Fig/chapter2-fig9.pdf

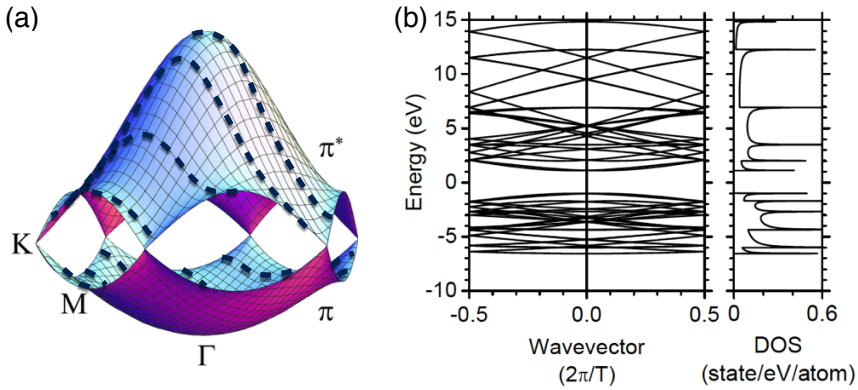

Figure 2.10: (a) The electronic dispersion relations of a graphene with the cutting lines (the dotted lines) for a semiconducting (4, 2) SWNT. (b) The electronic dispersion relations of the (4, 2) SWNT when different cutting lines are folded together into the 1D Brillouin zone. The length of the 1D Brillouin zone is given by $2\pi/T$. (c) The density of electronic states (DOS) of the (4, 2) SWNT. The sharp spikes in the DOS typical for 1D systems are known as Van Hove singularities [28].

Considering the the projection of the vector $\mathbf{\Gamma K}$ pointing towards the K point on the $\mathbf{K}_1$ direction normal to the cutting lines. Choosing the right top corner of the shaded hexagon in Fig. 2.9 (a) gives $\mathbf{\Gamma K} = (2\mathbf{b}_1 + \mathbf{b}_2)/3$. Using the expression for $\mathbf{K}_1$ in Eq. (2.59), we then find the projection $\mathbf{\Gamma K} \cdot \mathbf{K}_1)/|\mathbf{K}_1| = (2n + m)/3$. If $(2n + m)/3$ is an integer (i.e. $\mod(2n + m, 3) = 0$), ($\mathbf{\Gamma K}$ has an integer number of $\mathbf{K}_1$ components, so that one of the cutting lines crosses the K point, and the SWNT turns out to be metal. If $(2n + m)/3$ is a fractional number, namely 1/3 or 2/3 (i.e. $\mod(2n + m, 3) = 1$ or 2), none of the cutting lines crosses the K point and the SWNT becomes semiconductor. Fig. 2.9 (b) shows three types of SWNTs depending on the value of $\mod(2n + m, 3)$, which are referred to as M-, S1-, and S2-SWNT, respectively.

The electronic structure of SWNTs comprise 2N energy bands which originate from $N_{\rm hex}$ segments of cutting lines with each cutting line gives bonding π and anti-bonding π^* bands. Energy dispersion relation thus is plotted as a function of quasi-continuous $\mathbf{k}$ wavevector along $\mathbf{K}_2$. Figure 2.10 (a) and (b) show the cutting lines of the semiconducting (4, 2) SWNT with their corresponding energy dispersion. The electronic density of states (DOS), $g(E)$, is defined by the number of available electronic states for a given energy interval on units of states/1C-atom/eV. As discussed in Sec. 2.1, in the one-dimensional (1D) SWNT, $g(E) \propto (E - E_0)^{-1/2}$ diverges at some points known as Van Hove singularity points (VHS). Figure 2.10 (c) shows the DOS of the semiconducting (4, 2) SWNT. Vanishing DOS at the Fermi level $E_{\rm F} = 0$ eV indicates that the (4, 2) SWNT is a semiconductor.

Fig. 2.10: Fig/chapter2-fig10.pdf

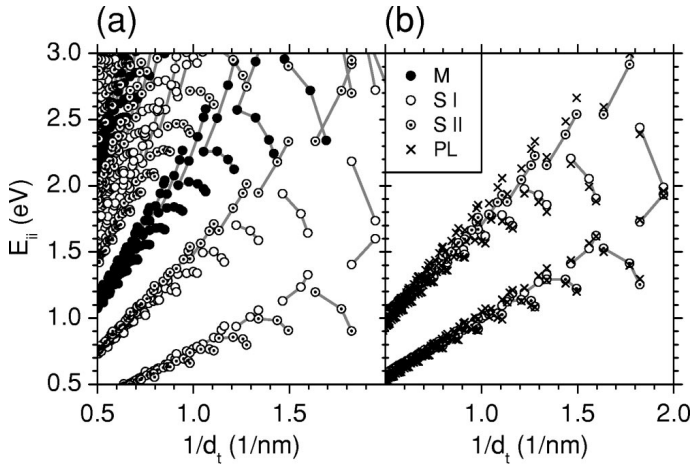

Figure 2.11: (a) Kataura plot of transition energies for metallic (closed dots) and semiconducting type I (open dots) and type II (marked dots) SWNTs based on the extended tight-binding (ETB) model [29]. (b) Comparison between the ETB calculations with the photoluminiscence empirical fit (crosses) [30].

2.2.5 Extended tight-binding model

Even though simple tight-binding (STB) model gives a good understanding towards electronic property of SWNTs, recent measurements of E_{ii} energy by photoluminiscence and resonance Raman spectroscopy indicate that the STB calculation is not sufficient to interpret the experimental results of many SWNTs [31, 30]. To clarify the origin of this problem, we reconsider the limitations of the STB model discussed previously. Within the STB model, the long-range atomic interactions and the effect of the curvature of the cylindrical surface of a SWNT are both neglected. The long-range atomic interactions are known to change the electronic energy band structure of the graphene and SWNTs. On the other hand, if we consider the effect of curvature, the π orbitals are mixed with the σ orbitals. Furthermore, the $\pi-\sigma$ rehybridization suggests that the geometrical structure of a small diameter SWNT deviates from the rolled up graphene. A geometrical structure optimization must thus be performed to allow for atomic relaxation to equilibrium positions. This in turn affects the E_{ii} energies of the small diameter SWNTs in the experimental results [31, 30]. In the case of large diameter SWNTs, however, the σ molecular orbitals are irrelevant because the surface is flat and thus the π and σ molecular orbitals are orthogonal to each other. Therefore, the STB model is now extended by including the long-range atomic interactions and the σ molecular orbitals, and by optimizing the geometrical structure. The resulting model is referred to as the extended tight-binding model (ETB). Within the framework of the ETB model, we use the tight-binding parametrization determined from density-

Fig. 2.11: Fig/chapter2-fig11.pdf

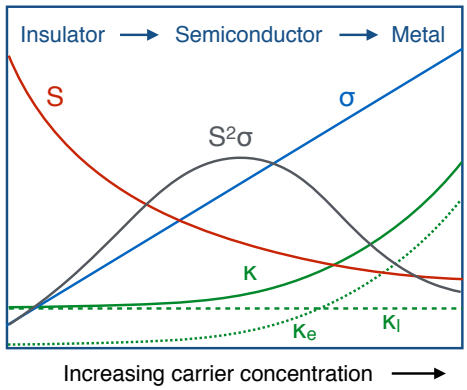

Figure 2.12: Schematic dependence of thermoelectric properties on charge-carrier concentration.

functional theory (DFT) employing the local-density approximation (LDA) and using a local orbital basis set [32]. The ETB model is developed by Samsonidze et. al [29]. Figure 2.10 (a) show the calculated ETB for E_{ii} of the SWNTs as a function of inverse diameter, which is often referred to as the Kataura plot [33]. By comparing it to the photoluminiscence empirical fit [30] we found that the results observed in the photoluminiscence studies is closely reproduced by the ETB approximation. The ETB model thus provides the proper chirality and the diameter dependence for the E_{ii} of the SWNTs. We note that E_{11} value is band gap for the semiconducting SWNT, which is important parameter to study the transport properties in the semiconducting SWNT.

2.3 Thermoelectric transport

In this section we discuss some of the thermoelectric transport properties for the semiconductors. Thermoelectric problem is generally interdependent between three parameters: the thermopower S, the electrical conductivity σ, and thermal conductivity κ, consists of constitutes the electronic κ_e and lattice κ_l contributions to thermal conductivity ($\kappa = \kappa_e + \kappa_l$). As discussed in Chapter 1, to obtain the high figure-of-merit $ZT = S^2\sigma\kappa^{-1}T$ and the high output power density $Q = \frac{1}{4h_l}S^2\sigma(T_h - T_c)^2$, thermoelectric materials should have a large S, large σ, and small κ. Unfortunately, there is difficult to find the materials that unusual combination of transport properties can be gained. For example, metals such as copper have large σ but small S and large κ due to a large electron concentration. Diamond, which is a insulator, has large S but small σ and large κ, the latter being due to a large lattice contribution. These materials properties are summarized in Fig. 2.12, which illustrates that the thermoelectric power factor $PF = S^2\sigma$ can be maximized for doped semiconductors.

Fig. 2.12: Fig/chapter2-fig12.pdf

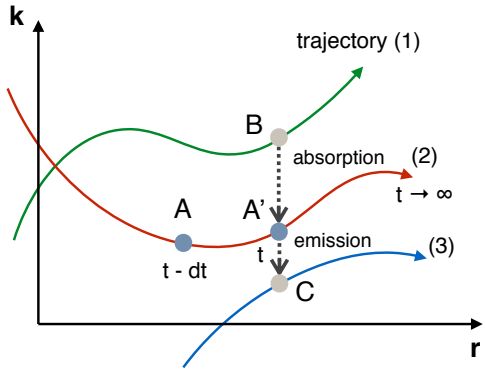

Figure 2.13: Illustration of trajectories in position-momentum space. Carriers move along a trajectory according to Newton's laws. Scattering changes the carrier's momentum, but does not affect its position.

Therefore, studying the transport properties for the semiconductors is important to improve the thermoelectricity.

An intrinsic semiconductor at $T = 0$ has no carriers and therefore there is no transport of carriers under the influence of external fields. However at finite temperatures there are thermally excited carriers. For finite electric fields, the electrical conductivity depends on the product of the carrier density and the carrier mobility. To the extent that electrons can be considered as particles, the electrical conductivity, the electronic contribution to the thermal conductivity are expressed by solving the Boltzmann equation.

2.3.1 Boltzmann transport formalism

A distribution function $f(\mathbf{r}, \mathbf{k}, t)$ is the probability of occupation of a carrier (electron or hole) at time $t + \mathrm{d}t$ at $\mathbf{r} + \mathrm{d}\mathbf{r}$ with wavevector lying between $\mathbf{k}$, $\mathbf{k} + \mathrm{d}\mathbf{k}$. Under equilibrium (i.e. no external electric or magnetic field and no thermal gradients), the distribution function is found from quantum-statistical analysis to be given by the Fermi-Dirac function for fermions

$$f_0(E) = \frac{1}{1 + e^{\frac{E(\mathbf{k}) - \mu(\mathbf{r})}{k_\mathrm{B} T(\mathbf{r})}}}, \tag{2.75}$$

where $E(\mathbf{k})$ is the energy of the electron, $\mu(\mathbf{r})$ is the chemical potential, $T(\mathbf{r})$ is the absolute temperature as a function of position $\mathbf{r}$, and k_B is the Boltzmann constant. It is known that the transport properties of solids are closely related to the energy dispersion relations $E(\mathbf{k})$ in these materials and in particular to the behavior of $E(\mathbf{k})$ near the Fermi energy.

Fig. 2.13: Fig/chapter2-fig13.pdf

Under an external perturbation such as an electric field or a thermal gradients, the carriers in a semiconductor move and change momentum in its trajectory $[\mathbf{r}(t),\ \mathbf{k}(t)]$. Figure 2.13 show several trajectories in position-momentum space. Consider a carrier at position A′ on trajectory 2 at time t, which before were at position A at time $t-\mathrm{d}t$. There are three processes under a carrier moving from A to A′: the diffusion, the effect of external forces and the collisions.

Let us take a fixed $\mathbf{k}$, one can say that the carriers in the small volume $\mathrm{d}\mathbf{r}$ at position $\mathbf{r}$ at time t are those who were at the position $\mathbf{r}-\mathbf{v}\mathrm{d}t$ at time $t-\mathrm{d}t$, where $\mathbf{v}=\mathrm{d}\mathbf{r}/\mathrm{d}t$ is the velocity of a carrier. The probability of occupation of a carrier at time t is the probability of occupation of a carrier at time $t-\mathrm{d}t$ earlier. So $f(\mathbf{r},\mathbf{k},t)=f(\mathbf{r}-\mathbf{v}\mathrm{d}t,\mathbf{k},t-\mathrm{d}t)=f(\mathbf{r},\mathbf{k},t-\mathrm{d}t)-\mathbf{v}\frac{\partial f}{\partial \mathbf{r}}\mathrm{d}t$. We can write this as

$$\left.\frac{\partial f}{\partial t}\right|_{\text{diffusion}}=-\mathbf{v}\frac{\partial f}{\partial \mathbf{r}}. \tag{2.76}$$

Likewise at a fixed position $\mathbf{r}$, one can say that the carriers of wavevector $\mathbf{k}$ are those who had wavevector $\mathbf{k}-\frac{\partial \mathbf{k}}{\partial t}\mathrm{d}t$ at time $t-\mathrm{d}t$. So $f(\mathbf{r},\mathbf{k},t)=f(\mathbf{r},\mathbf{k}-\frac{\partial \mathbf{k}}{\partial t}\mathrm{d}t,t-\mathrm{d}t)=f(\mathbf{r},\mathbf{k},t-\mathrm{d}t)-\frac{\partial \mathbf{k}}{\partial t}\frac{\partial f}{\partial \mathbf{k}}\mathrm{d}t$. We can write this as

$$\left.\frac{\partial f}{\partial t}\right|_{\text{fields}}=-\frac{\partial \mathbf{k}}{\partial t}\frac{\partial f}{\partial \mathbf{k}}. \tag{2.77}$$

Finally, we obtain the Boltzmann equation as

$$\begin{aligned}\frac{\partial f}{\partial t}&=\left.\frac{\partial f}{\partial t}\right|_{\text{diffusion}}+\left.\frac{\partial f}{\partial t}\right|_{\text{fields}}+\left.\frac{\partial f}{\partial t}\right|_{\text{collisions}}\\&=-\mathbf{v}\frac{\partial f}{\partial \mathbf{r}}-\frac{\partial \mathbf{k}}{\partial t}\frac{\partial f}{\partial \mathbf{k}}+\left.\frac{\partial f}{\partial t}\right|_{\text{collisions}}.\end{aligned} \tag{2.78}$$

Boltzmann equation is usually solved using following two approximations:

1. The perturbation due to external fields and forces is assumed to be small so that the distribution function can be linearized and written as

$$f=f_0+f_1, \tag{2.79}$$

where $f_0(E)$ is the equilibrium distribution function in Eq. (2.75), while $f_1(\mathbf{r},\mathbf{k})$ is the perturbation term.

2. The collision term in the Boltzmann equation is written in the relaxation time approximation (RTA) so that the system returns to equilibrium uniformly

$$\left.\frac{\partial f}{\partial t}\right|_{\text{collisions}}=-\frac{f-f_0}{\tau}=-\frac{f_1}{\tau}, \tag{2.80}$$

where τ is the relaxation time and in general is a function of wavevector $\mathbf{k}$, i.e., $\tau=\tau(\mathbf{k})$. The physical interpretation of τ is the time associated with the

rate of return to the equilibrium distribution when the external fields or thermal gradients are turned off. We consider a system when the fields are turned off at $t = 0$ (i.e. no diffusion and no effect of forces and fields), the Boltzmann equation in Eq. (2.78) becomes

$$\frac{\partial f}{\partial t} = \left.\frac{\partial f}{\partial t}\right|_{\text{collisions}} = -\frac{f - f_0}{\tau}, \tag{2.81}$$

which has solutions

$$f(t) = f_0 + \big(f(0) - f_0\big)e^{-t/\tau}, \tag{2.82}$$

where f_0 is the equilibrium distribution and $f(0)$ is the distribution function at time $t = 0$. This result suggests that any perturbation in the system will decay exponentially by a characteristic time constant τ.

With these approximations, the Boltzmann equation in Eq. (2.78) can be rewritten as

$$\frac{\partial(f_0 + f_1)}{\partial t} = -\mathbf{v}\frac{\partial(f_0 + f_1)}{\partial \mathbf{r}} - \frac{\partial \mathbf{k}}{\partial t}\frac{\partial(f_0 + f_1)}{\partial \mathbf{k}} - \frac{f_1}{\tau}. \tag{2.83}$$

When the distribution function reaches a steady state and considered uniform systems so that there is no gradient of f_1 with respect to $\mathbf{r}$, $\mathbf{k}$, and t, then Eq. (2.83) can be rewritten as

$$\frac{f_1}{\tau} = -\mathbf{v}\frac{\partial f_0}{\partial \mathbf{r}} - \frac{\partial \mathbf{k}}{\partial t}\frac{\partial f_0}{\partial \mathbf{k}}. \tag{2.84}$$

Using the definition of the electric force $\mathcal{F} = \hbar \mathrm{d}\mathbf{k}/\mathrm{d}t = q\mathcal{E}$, where $q = \pm e$ is the unit carrier charge and $\mathcal{E}$ is the electric field. The Boltzmann equation is then obtained as

$$\frac{f_1}{\tau} = -\mathbf{v}\left(\frac{\partial \mu}{\partial \mathbf{r}}\frac{\partial f_0}{\partial \mu} + \frac{\partial T}{\partial \mathbf{r}}\frac{\partial f_0}{\partial T}\right) - \frac{q\mathcal{E}}{\hbar}\left(\frac{\partial E}{\partial \mathbf{k}}\frac{\partial f_0}{\partial E}\right). \tag{2.85}$$

Substituting Eq.(2.75) and using the definition of the velocity $\mathbf{v} = 1/\hbar(\partial E/\partial \mathbf{k})$ into Eq. (2.85), we get

$$f_1 = \tau \mathbf{v}\frac{\partial f_0}{\partial E}\left(\nabla\mu + \frac{E - \mu}{T}\nabla T - q\mathcal{E}\right). \tag{2.86}$$

Eq. (2.86) is the solution of the Boltzmann equation and it applies equally well for holes and electrons in a semiconductor.

2.3.2 One-band model

The number of charge carriers per unit volume in the range of energy from E to $E + \mathrm{d}E$ is $f_1 g(E)\mathrm{d}E$, where f_1 is the occupation probability of a carrier that given by Eq. (2.86), and $g(E)$ is the density of state (DOS). Because the carriers, with charge $q = -e$ for the electron and $q = +e$ for the hole, move in the i^{th} direction with a velocity v_i, the electric current density $\mathcal{J}$ is given by

$$\mathcal{J} = \int q\mathbf{v} f_1 g(E)\mathrm{d}E. \tag{2.87}$$

Since $E-\mu$ represents the total energy transported by a carrier, the flux of the energy $\mathcal{W}$ is given by

$$\mathcal{W} = \int (E-\mu)\mathbf{v}f_1 g(E)\mathrm{d}E. \tag{2.88}$$

By inserting Eq.(2.86) into Eq.(2.87), we find that

$$\mathcal{J} = \int q\mathbf{v}\tau\mathbf{v}\frac{\partial f_0}{\partial E}\left(\nabla\mu + \frac{E-\mu}{T}\nabla T - q\mathcal{E}\right) g(E)\mathrm{d}E, \tag{2.89}$$

and

$$\mathcal{W} = \int (E-\mu)\mathbf{v}\tau\mathbf{v}\frac{\partial f_0}{\partial E}\left(\nabla\mu + \frac{E-\mu}{T}\nabla T - q\mathcal{E}\right) g(E)\mathrm{d}E. \tag{2.90}$$

To find an expression for the electrical conductivity, we set a zero temperature gradient $\nabla T = 0$ and a zero carrier concentration gradient $\nabla\mu = 0$, so that the electrical conductivity tensor σ is expressed by

$$\sigma = \frac{\mathcal{J}}{\mathcal{E}} = \int -q^2\mathbf{v}\tau\mathbf{v}\frac{\partial f_0}{\partial E} g(E)\mathrm{d}E. \tag{2.91}$$

Using the definition of the electric field $\mathcal{E} = -\nabla\varphi(\mathbf{r})$ and the chemical potential $\mu(\mathbf{r}) = \Phi - q\varphi(\mathbf{r})$, where Φ is the electrochemical potential, and $\varphi(\mathbf{r})$ is the electrostatic potential energy, Eq. (2.88) can be rewritten as

$$\mathcal{J} = \int q\mathbf{v}\tau\mathbf{v}\frac{\partial f_0}{\partial E}\left(\nabla\Phi + \frac{E-\mu}{T}\nabla T\right) g(E)\mathrm{d}E. \tag{2.92}$$

For the thermopower, we set a non-zero temperature gradient $\nabla T \neq 0$, when the circuit is open and no electric current flows (i.e. $\mathcal{J} = 0$ in Eq. (2.92)), then we obtain the thermopower tensor S from Eq. (2.92) as

$$S = -\frac{\nabla V}{\nabla T} = -\frac{1}{q}\frac{\nabla\Phi}{\nabla T} = \frac{1}{qT}\frac{\displaystyle\int q\mathbf{v}\tau\mathbf{v}\frac{\partial f_0}{\partial E}(E-\mu)g(E)\mathrm{d}E}{\displaystyle\int q\mathbf{v}\tau\mathbf{v}\frac{\partial f_0}{\partial E}g(E)\mathrm{d}E}. \tag{2.93}$$

The electronic thermal conductivity tensor κ_e can be found with no current flows (i.e. $\mathcal{J} = 0$). Using Eq. (2.90), we get

$$\kappa_e = -\frac{\mathcal{W}}{\nabla T} = -\frac{1}{T}\left[\int \mathbf{v}\tau\mathbf{v}\frac{\partial f_0}{\partial E}(E-\mu)^2 g(E)\mathrm{d}E + \frac{\left(\displaystyle\int \mathbf{v}\tau\mathbf{v}\frac{\partial f_0}{\partial E}(E-\mu)g(E)\mathrm{d}E\right)^2}{\displaystyle\int \mathbf{v}\tau\mathbf{v}\frac{\partial f_0}{\partial E}g(E)\mathrm{d}E}\right]. \tag{2.94}$$

All of the integrals that appear in Eqs. (2.91), (2.93), and (2.94) have the same general form. They may be expressed conveniently as

$$\mathcal{L}_\alpha = \int -q^2\mathbf{v}\tau\mathbf{v}\frac{\partial f_0}{\partial E}(E-\mu)^\alpha g(E)\mathrm{d}E. \tag{2.95}$$

Thus, the transport coefficients σ, S, and κ_e within the one-band model can be written in terms of the integrals $\mathcal{L}_\alpha$ as

$$\sigma = \mathcal{L}_0, \tag{2.96}$$

$$S = \frac{1}{qT}\frac{\mathcal{L}_1}{\mathcal{L}_0}, \tag{2.97}$$

$$\kappa_e = \frac{1}{q^2T}\left(\mathcal{L}_2 - \frac{\mathcal{L}_1^2}{\mathcal{L}_0}\right). \tag{2.98}$$

The calculation of Eq. (2.95) requires knowledge of the carrier velocity $\mathbf{v}(E)$ of the energy band, the relaxation time $\tau(E)$, and the density of state $g(E)$, which defined for any semiconductors (Eqs. (2.27), (2.36), and (2.46) for 3D, 2D, and 1D, respectively).

$$\mathbf{v}^2(E) = \frac{2E}{m^*D}, \tag{2.99}$$

$$\tau(E) = \tau_0\left(\frac{E}{k_\mathrm{B}T}\right)^r, \tag{2.100}$$

$$g(E) = \frac{1}{L^{3-D}2^{D-1}\pi^{D/2}\Gamma\left(\frac{D}{2}\right)}\left(\frac{2m^*}{\hbar^2}\right)^{D/2}E^{D/2-1}, \tag{2.101}$$

where $D = 1,\ 2,\ 3$ denotes the dimension of the material, m^* is the effective mass of electrons or holes, r is a characteristic exponent, τ_0 is the relaxation time constant, and L is the confinement length for a particular material dimension.

Substituting Eqs. (2.99)-(2.101) into Eq. (2.95) yields

$$\begin{aligned}\mathcal{L}_\alpha = {} & \frac{-4q^2\tau_0(m^*)^{D/2-1}}{DL^{3-D}(2\pi)^{D/2}\hbar^D\Gamma(\frac{D}{2})(k_\mathrm{B}T)^r} \\ & \times\int\frac{\partial f_0}{\partial E}E^{r+D/2}\left[E^\alpha - \begin{pmatrix}\alpha\\1\end{pmatrix}E^{\alpha-1}\mu + \begin{pmatrix}\alpha\\2\end{pmatrix}E^{\alpha-2}\mu^2 + \ldots\right]\mathrm{d}E,\end{aligned} \tag{2.102}$$

where

$$\begin{pmatrix}\alpha\\n\end{pmatrix} = C_n^\alpha = \frac{\alpha!}{n!(\alpha-n)!} \quad \text{for} \ \ 0 \le n \le \alpha, \tag{2.103}$$

which is a specific positive integer known as a binomial coefficient. The integrals term in Eq. (2.102) can be simplified using the product rule as

$$\int\frac{\partial f_0}{\partial E}E^j\mathrm{d}E = f_0E^j\big|_0^\infty - j\int f_0E^{j-1}\mathrm{d}E = -j\int f_0E^{j-1}\mathrm{d}E. \tag{2.104}$$

Then using the reduced band energy $\xi = E/k_\mathrm{B}T$ and the reduced chemical potential $\eta = \mu/k_\mathrm{B}T$, so that

$$\int\frac{\partial f_0}{\partial E}E^j\mathrm{d}E = -j(k_\mathrm{B}T)^j\int f_0\xi^{j-1}\mathrm{d}\xi = -j(k_\mathrm{B}T)^jF_{j-1}, \tag{2.105}$$

where

$$F_j = \int f_0\xi^j\mathrm{d}\xi, \tag{2.106}$$

which is called the Fermi-Dirac integral. Inserting Eq. (2.105) into Eq. (2.102) we get after some calculation

$$\begin{aligned}\mathcal{L}_\alpha = \frac{-4q^2\tau_0(m^*)^{D/2-1}(k_\mathrm{B}T)^{D/2+\alpha}}{DL^{3-D}(2\pi)^{D/2}\hbar^D\Gamma(\frac{D}{2})}\Bigg[&-(r+\frac{D}{2}+\alpha)F_{r+D/2+\alpha-1}\\ &+\eta\begin{pmatrix}\alpha\\1\end{pmatrix}(r+\frac{D}{2}+\alpha-1)F_{r+D/2+\alpha-2}\\ &-\eta^2\begin{pmatrix}\alpha\\2\end{pmatrix}(r+\frac{D}{2}+\alpha-2)F_{r+D/2+\alpha-3}+\ldots\Bigg],\end{aligned} \tag{2.107}$$

where η denotes the reduced chemical potential. Substituting Eq. (2.107) with $\alpha = 0$ and 1 into Eqs. (2.96) and (2.97) we obtain the following formula for σ and S as

$$\sigma = \mathcal{L}_0 = \frac{4q^2\tau_0(m^*)^{D/2-1}(k_\mathrm{B}T)^{D/2}\left(r+\frac{D}{2}\right)}{DL^{3-D}(2\pi)^{D/2}\hbar^D\Gamma(\frac{D}{2})}F_{r+D/2-1}, \tag{2.108}$$

and

$$S = \frac{1}{qT}\frac{\mathcal{L}_1}{\mathcal{L}_0} = -\frac{k_\mathrm{B}}{q}\left(\eta - \frac{\frac{d}{2}+r+1}{\frac{d}{2}+r}\times\frac{F_{d/2+r}}{F_{d/2+r-1}}\right). \tag{2.109}$$

Now we consider the nondegenerate semiconductors that is applicable when $\eta \ll 0$. In this case, the Fermi level lies within the band gap, we can thus use an approximation

$$\begin{aligned}F_j &= \int f_0\xi^j\mathrm{d}\xi = \int\frac{1}{e^{\xi-\eta}+1}\xi^j\mathrm{d}\xi\\ &\approx \int\frac{1}{e^{\xi-\eta}}\xi^j\mathrm{d}\xi = e^\eta\int e^{-\xi}\xi^j\mathrm{d}\xi = e^\eta\Gamma(j+1),\end{aligned} \tag{2.110}$$

where $\Gamma(j) = \int e^{-\xi}\xi^j\mathrm{d}\xi$ is the Gamma function. Eqs. (2.108) and (2.109) become

$$\sigma = \frac{4q^2\tau_0(m^*)^{D/2-1}(k_\mathrm{B}T)^{D/2}\left(r+\frac{D}{2}\right)\Gamma(\frac{D}{2}+r)}{DL^{3-D}(2\pi)^{D/2}\hbar^D\Gamma(\frac{D}{2})}e^\eta, \tag{2.111}$$

and

$$S = -\frac{k_\mathrm{B}}{q}\left(\eta - \frac{\frac{d}{2}+r+1}{\frac{d}{2}+r}\times\frac{\Gamma(\frac{D}{2}+r+1)}{\Gamma(\frac{D}{2}+r)}\right). \tag{2.112}$$

Using the recursion formula $\Gamma(j+1) = j\Gamma(j)$, Eq. (2.112) can be simply written as

$$S = -\frac{k_\mathrm{B}}{q}\left(\eta - \frac{D}{2} - r - 1\right). \tag{2.113}$$

It is conventional to describe κ_e in terms of the Lorenz number L, which defined as $L = \kappa_e/\sigma T$. Then, from Eqs. (2.96) and (2.98),

$$L = \frac{1}{(qT)^2}\left(\frac{\mathcal{L}_2}{\mathcal{L}_0} - \frac{\mathcal{L}_1^2}{\mathcal{L}_0^2}\right) = \left(\frac{k_\mathrm{B}}{q}\right)^2\left(r+\frac{D}{2}+2\right). \tag{2.114}$$

We see that L is independent of the Fermi energy, but depends on the exponent r and the dimension D in Eq. (2.100) for the nondegenerate semiconductors.

Now we turn to the degenerate semiconductors when $\eta/k_{\mathrm{B}}T \gg 0$. This means that the Fermi level lies above the conduction-band bottom for electrons or below the valence-band top for holes. In this case, the conductor is metallic. Thus, the Fermi-Dirac integral can be expressed in the form of a rapidly converging series

$$\begin{aligned} F_j &= \int f_0 \xi^j \mathrm{d}\xi = -\frac{1}{j+1}\int \frac{\partial f_0}{\partial \xi}\xi^{j+1}\mathrm{d}\xi \\ &= -\frac{1}{j+1}\int \frac{\partial f_0}{\partial \xi}\left[\eta^{j+1} + \begin{pmatrix} j \\ 1 \end{pmatrix}\eta^j(\xi-\eta) + \begin{pmatrix} j \\ 2 \end{pmatrix}\eta^{j-1}(\xi-\eta)^2 + \ldots\right]\mathrm{d}\xi \\ &= \frac{\eta^{j+1}}{j+1} + j\eta^{j-1}\frac{\pi^2}{6} + j(j-1)(j-2)\eta^{j-3}\frac{7\pi^4}{360} + \ldots. \end{aligned} \tag{2.115}$$

The electrical conductivity of the degenerate semiconductor is found by inserting only the first term in Eq. (2.115) into Eq. (2.108),

$$\sigma = \frac{4q^2\tau_0(m^*)^{D/2-1}(k_{\mathrm{B}}T)^{D/2}}{DL^{3-D}(2\pi)^{D/2}\hbar^D\Gamma(\frac{D}{2})}\eta^{r+D/2}. \tag{2.116}$$

On the other hand, if only the first term in Eq. (2.115) is used, the thermopower in Eq. (2.109) would be zero, which is consistent with the fact that most metals have negligibly small values of the thermopower. To obtain a nonzero value for the thermopower, the first two terms of Eq. (2.115) are used. Then we obtain

$$S = \frac{k_{\mathrm{B}}}{q}\frac{\pi^2}{3}\frac{\left(r+\frac{D}{2}\right)}{\eta}. \tag{2.117}$$

The first two terms are also needed to obtain the Lorenz number, which is given by

$$L = \frac{\pi^2}{3}\left(\frac{k_{\mathrm{B}}}{q}\right)^2 = 2.44\times10^{-8}\ \mathrm{W\Omega K^{-2}}. \tag{2.118}$$

This shows that the Lorenz number is constant for strongly degenerate system and, in particular, it should not depend on the scattering mechanisms or the dimensional materials. These features agree with the well-established Wiedemann-Franz-Lorenz law which states that the ratio of the electronic contribution of the thermal conductivity to electrical conductivity of a metal is proportional only to the absolute temperature, and does not depend on materials.

2.3.3 Multi-band effect

In 1D nanowire with large width or 2D layer with large thickness, there are many energy subbands that need to be taken into consideration due to the degeneracy of

the multiple carrier pockets at the conduction band and valence band extrema for a given energy (see Figs. 2.3 and 2.4). For a low-dimensional system, besides the degeneracy effect, quantum confinement also introduces band splitting, and results in a set of subbands that comes from a single band of the bulk materials. In such a case, the one-band model does not work well to describe the thermoelectricity of the low-dimensional systems. Therefore, contributions from all of the subbands with band extrema that fall within a few $k_{\mathrm{B}}T$ window around the Fermi energy need to be included for the calculation of S, σ, and κ_e. For a multi-band system, Eqs. (2.96)-(2.98) needs to be replaced by sum $\mathcal{L}_{\alpha,\mathrm{total}} = \sum_b \mathcal{L}_\alpha^b$ of contributions from each subband b, and the quantities of transports coefficients, we finally get

$$\sigma_{\mathrm{total}} = \sum_b \mathcal{L}_0^b, \tag{2.119}$$

$$S_{\mathrm{total}} = \frac{1}{qT} \frac{\sum_b \mathcal{L}_1^b}{\sum_b \mathcal{L}_0^b}, \tag{2.120}$$

$$\kappa_{e,\mathrm{total}} = \frac{1}{q^2 T} \left(\sum_b \mathcal{L}_2^b - \frac{\left(\sum_b \mathcal{L}_1^b \right)^2}{\sum_b \mathcal{L}_0^b} \right). \tag{2.121}$$

The important example is to find the optimum thermopower values of semi-metal or narrow-gap semiconductors in which there are significant contributions from both the electrons in the conduction band and holes in the valence band. Another example is found when there are comparable numbers of carriers of the same sign with different effective masses, such as the light and heavy holes in p-type silicon. We now consider the thermopower of multi-band to find the optimum thermopower values. We assumed that there are two bands (one band from the conduction band and another one band from the valence band) that make a significant contribution in the thermopower. We thus obtain thermopower of two-band from Eqs. (2.119) and (2.120)

$$S = \frac{\sigma_n S_n + \sigma_p S_p}{\sigma_n + \sigma_p}, \tag{2.122}$$

where $\sigma_{n,p}$ and $S_{n,p}$ are the electrical conductivity and thermopower of the electron ($q = -e$) and hole ($q = +e$) for the one-band model, respectively. For the nondegenerate semiconductors, substituting $\sigma_{n,p}$ in Eq. (2.111) and $S_{n,p}$ in Eq. (2.113) into Eq. (2.122) yields

$$S = \frac{k_{\mathrm{B}}}{e} \frac{\left(\eta_n - \frac{D}{2} - r - 1 \right) \frac{\sigma_n}{\sigma_p} - \left(\eta_p - \frac{D}{2} - r - 1 \right)}{\frac{\sigma_n}{\sigma_p} + 1}. \tag{2.123}$$

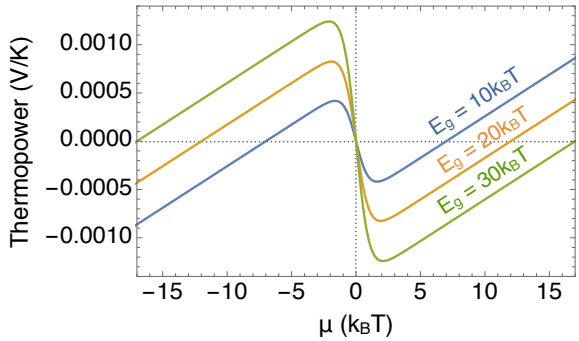

Figure 2.14: Thermopower S of two bands as a function of the chemical potential μ and the energy band gap E_g ($A = 1$, $r = -1/2$, and $D = 3$).

where $\sigma_n/\sigma_p = \left(m_n^*/m_p^*\right)^{D/2-1} e^{\eta_n - \eta_p} = Ae^{\eta_n - \eta_p}$, with $A = \left(m_n^*/m_p^*\right)^{D/2-1}$, where m_n^* and m_p^* are the effective masses for electron and hole of conduction band and valence band, respectively. Here we have $\eta_n - \eta_p = 2\mu/(k_{\mathrm{B}}T)$ and $\eta_n + \eta_p = -E_g/(k_{\mathrm{B}}T)$, where μ is the Fermi level and E_g is the energy band gap. The thermopower of the nondegenerate semiconductors within the two-band approximation can then be written in terms of μ, E_g, r, D, and A from Eq. (2.123) as

$$S = \frac{k_B}{e}\left(\frac{\mu}{k_{\mathrm{B}}T} - \frac{E_g}{2k_{\mathrm{B}}T} - r - \frac{D}{2} - 1 + \frac{E_g/k_{\mathrm{B}}T + 2r + D + 2}{Ae^{2\mu/k_{\mathrm{B}}T} + 1}\right). \tag{2.124}$$

If we suppose for the moment that A is equal to unity, S will be zero when the Fermi level is at the center of the energy gap ($\mu = 0$). On the other hand, as the Fermi level moves just a few $k_{\mathrm{B}}T$ toward the conduction band or valence band edges, the ratio of the electron to hole concentration becomes very large or very small and the thermopower is dominated by the contribution from one carrier or the other, as shown in Fig. 2.14. Therefore, the optimum thermopower is clearly quite close to S from one carrier at $\mu = 0$ or $\eta_{n,p} = -E_g/2k_{\mathrm{B}}T$, which is

$$S_{\mathrm{opt}} = \frac{k_{\mathrm{B}}}{q}\left(\frac{E_g}{2k_{\mathrm{B}}T} + \frac{D}{2} + r + 1\right) \sim \frac{E_g}{2qT}. \tag{2.125}$$

We note that S in Eq. (2.113) is used in this case because the Fermi level lies within the energy band gap (i.e. the nondegenerate semiconductors). For a more practical argument for designing thermoelectric material, we can determine a condition to obtain an optimized Fermi level, which satisfies $\mathrm{d}S(\mu_{\mathrm{opt}})/\mathrm{d}\mu = 0$. In practice, we will discuss the optimized Fermi level and the optimized thermopower for many semiconducting carbon nanotubes with both analytical and numerical calculations in Chapter 4.

Fig. 2.14: Fig/chapter2-fig14.pdf

Chapter 3

Power factor of low-dimensional semiconductors

In this Chapter, we give an analytical formula for the optimum PF value which can show the interplay between the quantum confinement length and the thermal de Broglie wavelength in low-dimensional semiconductors (see an illustration in Fig. 3.1). We apply the one-band model (see in Chapter 2) with the relaxation time approximation (RTA) to derive the analytical formula for the PF of nondegenerate semiconductors. The justification for the one-band model with the RTA was already given in some earlier studies, which concluded that the model was accurate enough to predict the thermoelectric properties of low dimensional semiconductors, such as semiconducting carbon nanotubes (s-SWNTs) [34], Bi_2Te_3 thin films [7], and Bi nanowires [7, 35]. To obtain the PF formula in this work, we use similar analytical expressions for the Seebeck coefficient S and the electrical conductivity σ based on one-band model which were derived in Chapter 2.

3.1 Optimum power factor of non-degenerate semiconductors

As discussed earlier in Chapter 2, the thermopower (or the Seebeck coefficient) S and the electrical conductivity σ are given, respectively, by Eqs. (2.111) and (2.113) (see Ref. [34])

$$S = -\frac{k_{\mathrm{B}}}{q}\left(\eta - r - \frac{D}{2} - 1\right), \tag{3.1}$$

and

$$\sigma = \frac{4q^2\tau_0\left(r+\frac{D}{2}\right)(k_BT)^{D/2}\Gamma(r+\frac{D}{2})}{DL^{3-D}(2\pi)^{D/2}\hbar^D\Gamma(\frac{D}{2})}(m^*)^{D/2-1}e^{\eta}, \tag{3.2}$$

where $D = 1, 2, 3$ denotes the dimension of the material, $q = \pm e$ is the unit carrier charge, T is the average absolute temperature, m^* is the effective mass of electrons

Fig. 3.1: Fig/chapter3-fig1.pdf

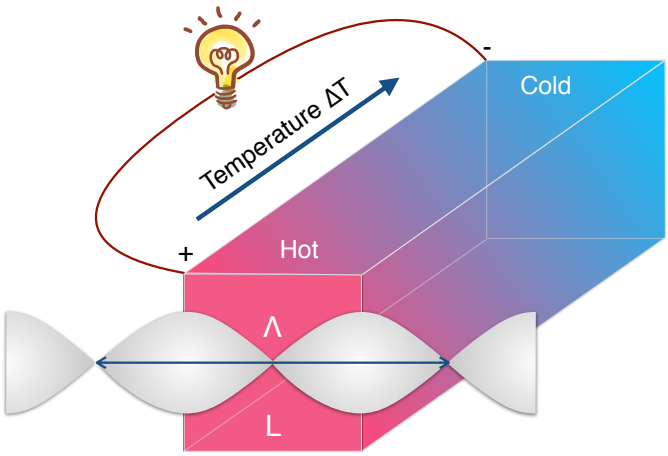

Figure 3.1: An illustration of the interplay between the quantum confinement length L and the thermal de Broglie wavelength Λ in low-dimensional materials.

or holes, τ_0 is the relaxation time coefficient, r is a characteristic exponent of the energy-dependent relaxation time $\tau(E)$ (see below), L is the confinement length for a particular material dimension, $\Gamma(t) = \int_0^\infty x^{t-1}e^{-x}\mathrm{d}x$ is the Gamma function, $\eta = \zeta/k_\mathrm{B}T$ is the dimensionless chemical potential (while ζ is defined as the chemical potential measured from top of the valence energy band in a p-type semiconductor), k_B is the Boltzmann constant, and $\hbar$ is the Planck constant. From Eqs. (3.1) and (3.2), the thermoelectric power factor can be written as

$$PF \equiv S^2\sigma = A(\eta - C)^2 e^\eta, \tag{3.3}$$

where A (in units of $\mathrm{W/mK^2}$) and C (dimensionless) are given by

$$A = \frac{4\tau_0 k_\mathrm{B}^2}{L^3 m^*}\left(\frac{L}{\Lambda}\right)^D \frac{\left(r+\frac{D}{2}\right)\Gamma\left(r+\frac{D}{2}\right)}{D\,\Gamma\left(\frac{D}{2}\right)}, \tag{3.4}$$

and

$$C = r + \frac{D}{2} + 1, \tag{3.5}$$

respectively, with $\Lambda = (2\pi\hbar^2/k_\mathrm{B}Tm^*)^{1/2}$ is known as the thermal de Broglie length, which is a measure of the thermodynamic uncertainty for the localization of a particle of mass m^* with the average thermal momentum $\hbar(2\pi/\Lambda)$ [36]. In Eq. (3.2) we consider an isotropic system in which the carrier relaxation time is assumed to follow a power law dependence on energy, i.e., $\tau(E) = \tau_0(E/k_\mathrm{B}T)^r$ [37, 38]. Note that the characteristic exponent, r, depends on the scattering mechanisms and the relaxation time coefficient, τ_0, has the units of time. For example, when the acoustic phonon scattering is considered to be the dominant scattering mechanism, then $r = +0.5$, $r = 0$, and $r = -0.5$ are typical values for $D = 1, 2, 3$ three materials, respectively [37, 38].

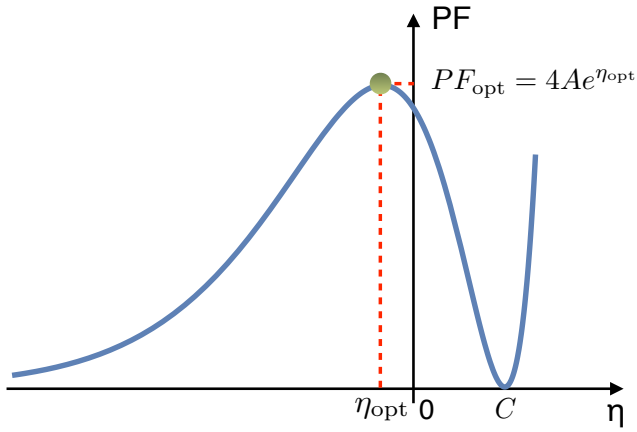

Figure 3.2: The power factor as a function of the reduced chemical potential η.

For a given $\tau(E)$, the carrier mobility is defined by

$$\mu = \frac{q\langle\langle\tau(E)\rangle\rangle}{m^*}, \tag{3.6}$$

where

$$\langle\langle\tau(E)\rangle\rangle \equiv \frac{\langle E\tau(E)\rangle}{\langle E\rangle}, \tag{3.7}$$

where $\langle x\rangle = \int_0^\infty xe^{-E/k_{\mathrm{B}}T}\mathrm{d}E$ is a canonical average of x. Here, the quantity $\langle\langle\tau(E)\rangle\rangle$ is introduced to make an energy-dependent relaxation time. When we insert $\tau(E)$ in power law form as $\tau(E) = \tau_0[E(\mathbf{k})/k_{\mathrm{B}}T]^r$ in Eq. (3.7), we find

$$\langle\langle\tau(E)\rangle\rangle = \tau_0\frac{\int_0^\infty(\mathbf{k}^2/2m^*k_{\mathrm{B}}T)^r e^{-\mathbf{k}^2/2m^*k_{\mathrm{B}}T}\mathbf{k}^4\mathrm{d}\mathbf{k}}{\int_0^\infty e^{-\mathbf{k}^2/2m^*k_{\mathrm{B}}T}\mathbf{k}^4\mathrm{d}\mathbf{k}}. \tag{3.8}$$

With the substitution, $y = \mathbf{k}^2/2m^*k_{\mathrm{B}}T$,

$$\langle\langle\tau(E)\rangle\rangle = \tau_0\frac{\int_0^\infty y^{r+3/2}e^{-y}\mathrm{d}y}{\int_0^\infty y^{3/2}e^{-y}\mathrm{d}y}. \tag{3.9}$$

After recalling the definition of the Gamma function, $\Gamma(t) = \int_0^\infty x^{t-1}e^{-x}\mathrm{d}x$, we can rewrite Eq. (3.7) as

$$\langle\langle\tau(E)\rangle\rangle = \tau_0\frac{\Gamma\left(\frac{5}{2}+r\right)}{\Gamma\left(\frac{5}{2}\right)}. \tag{3.10}$$

From Eqs. (3.4), (3.6) and (3.10), the term A of the power factor can be rewritten as

$$A = \frac{4\mu k_{\mathrm{B}}^2}{qL^3}\left(\frac{L}{\Lambda}\right)^D\frac{\left(r+\frac{D}{2}\right)\mathrm{B}\left(r,\frac{5}{2}\right)}{D\mathrm{B}\left(r,\frac{D}{2}\right)}, \tag{3.11}$$

Fig. 3.2: Fig/chapter3-fig2.pdf

where $\mathrm{B}(x,y) = \Gamma(x)\Gamma(y)/\Gamma(x+y)$ is the Beta function. We can now determine the optimum power factor as a function of η from Eq. (3.3) by solving $\mathrm{d}(PF)/\mathrm{d}\eta = 0$. The optimum power factor, PF_{opt}, and the corresponding value for the reduced (or dimensionless) chemical potential, η_{opt}, are given, respectively, by

$$PF_{\mathrm{opt}} = \frac{16\mu k_{\mathrm{B}}^2}{qL^3}\left(\frac{L}{\Lambda}\right)^D \frac{\left(r+\frac{D}{2}\right)\mathrm{B}\left(r,\frac{5}{2}\right)}{D\mathrm{B}\left(r,\frac{D}{2}\right)} e^{r+D/2-1}, \tag{3.12}$$

and

$$\eta_{\mathrm{opt}} = r + \frac{D}{2} - 1. \tag{3.13}$$

Figure 3.2 shows the power factor as a function of the dimensionless chemical potential η. Since η is measured from the top of the valence band, $\eta_{\mathrm{opt}} < 0$ ($\eta_{\mathrm{opt}} > 0$) corresponds to a condition in which the Fermi energy is located inside (outside) the energy band gap. Here we assume that the energy gap is much larger than $k_{\mathrm{B}}T$ for the non-degenerate semiconductors. For example, in the 1D system, if r and D are taken to be 0 and 1, respectively, Eq. (3.13) gives $\eta_{\mathrm{opt}} = -\frac{1}{2}$ which means that η_{opt} is located around $\frac{1}{2}k_{\mathrm{B}}T$ below the top of the valence band. Since the values of the characteristic exponent r in the description of $\tau(E)$ are ranging from -0.5 to 1.5 for various scattering processes [37, 38, 39, 40], we find that the range of the η_{opt} values would be $(-1,1)$, $(-\frac{1}{2},\frac{3}{2})$, and $(0,2)$ for the 1D, 2D, and 3D systems, respectively. Therefore, the small η_{opt} value will make position of the Fermi energy very close (within a few $k_{\mathrm{B}}T$) to the valence band edge for the p-type semiconductor [41]. It is noted that for an n-type semiconductor, we can redefine η or ζ to be measured from the bottom of the conduction band. We should be careful that if we consider 1D and 2D systems having quite large confinement length L such that many subbands contribute to the transport properties, the electronic density-of-states would resemble the 3D system [42]. In such a case, the one-band model does not work well to describe the thermoelectricity because several subband energies fall within a few $k_{\mathrm{B}}T$ window around the Fermi energy, which is beyond the scope of this work.

3.2 Effect of energy-dependent relaxation time on power factor

Next, we discuss some cases where the optimum power factor PF_{opt} may be enhanced significantly. Fig. 3.3 shows PF_{opt} as a function of the characteristic exponent r for the 1D, 2D, and 3D systems, in which the values of r range from -0.5 to 1.5 for various scattering processes [37, 38]. In these examples, we consider a typical semiconductor, n-type Si, at room temperature and high-doping concentrations on the order of 10^{18} cm^{-3}. The thermal de Broglie wavelength and the carrier mobility are set to be

Fig. 3.3: Fig/chapter3-fig3.pdf

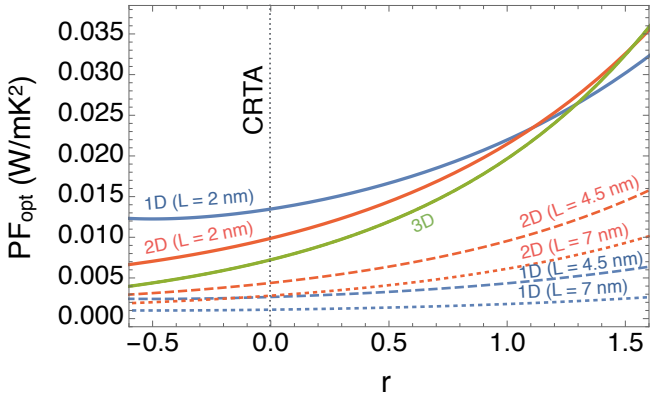

Figure 3.3: Optimum power factor as a function of characteristic exponent for the 1D, 2D, and 3D systems. The thermal de Broglie wavelength is set to be $\Lambda = 4.5$ nm (for n-type Si) and the mobility is $\mu = 420$ cm^2/Vs. The confinement length L is varied for the 1D and 2D systems, each for $L = 2$ nm, $L = \Lambda$ (4.5 nm), and $L = 7$ nm. The value of $r = 0$ corresponds to the constant relaxation time approximation (CRTA).

$\Lambda = 4.5$ nm and $\mu = 420$ cm^2/Vs, respectively. We note that the scattering time assumed under the constant relaxation time approximation (CRTA) corresponds to $r = 0$, and thus $\langle\langle \tau(E) \rangle\rangle \equiv \tau_0$ [43]. As shown in Fig. 3.3, $PF_{\rm opt}$ increases with increasing r for all the 1D, 2D, and 3D systems. The effect of the characteristic exponent r on the 3D system is stronger than that of the 1D and 2D systems. Based on Eq. (3.12) and Fig. 3.3, $PF_{\rm opt}$ increases with decreasing L which corresponds to the confinement effect for the 1D and 2D systems. It is noted in Fig. 3.3 that $PF_{\rm opt}$ in the 3D system does not depend on L as shown in Eq. (3.12) with $D = 3$. However, the qualitative behaviour between r and $PF_{\rm opt}$ is not much affected by changing L since r and L are independent of each other in Eq. (3.12).

3.3 Quantum and classical size effects on power factor

Figure 3.4 shows $PF_{\rm opt}$ as a function of confinement length L and thermal de Broglie wavelength Λ for the 1D, 2D, and 3D systems. The mobility is set to be $\mu = 420$ cm^2/Vs for all systems and the scattering rate may be proportional to be the density of final states. The assumption of proportionality of the scattering rate with respect to the density of states, the scattering rate corresponds to $r = +0.5$, $r = 0$ and $r = -0.5$ for 1D, 2D, and 3D systems, respectively [38]. The curves in the left and middle panel of Fig. 3.3 particularly show a L^{-2} and L^{-1} dependence of the power factor for 1D and 2D systems, respectively [Eq. (3.12)]. These results are in good agreement with the model by Hicks and Dresselhaus [7, 8]. It is important to point out that

Fig. 3.4: Fig/chapter3-fig4.pdf

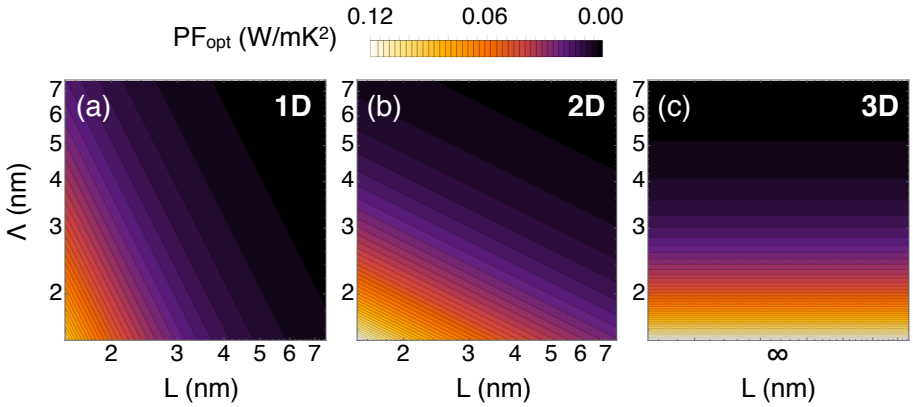

Figure 3.4: Optimum power factor $PF_{\rm opt}$ as a function of confinement length L and thermal de Broglie wavelength Λ for (a) 1D, (b) 2D, and (c) 3D systems.

the dependence of $PF_{\rm opt}$ on Λ also needs to be considered. For an ideal electron gas under the trapping potential, the thermodynamic uncertainty principle may roughly be expressed as $\Delta P/P \times \Delta V/V \geq (D^{3/2}/\sqrt{2\pi})\Lambda/L$, where P and V are the pressure and volume of the system, respectively (see in Appendix A). The uncertainty principle ensures that when the confinement length is comparable with the thermal de Broglie wavelength, i.e., $L \leq (D^{3/2}/\sqrt{2\pi})\Lambda$, the P and V cannot be treated as commuting observables. In this case, the quantum effects play an important role in increasing $PF_{\rm opt}$ for nanostructures. For the 1D system [Fig. 3.4 (a)] $PF_{\rm opt}$ starts to increase significantly when L is much smaller than Λ, while for the 2D system [Fig. 3.4 (b)] $PF_{\rm opt}$ starts to increase significantly when L is comparable to Λ. As for the 3D system [Fig. 3.4 (c)], $PF_{\rm opt}$ increases with decreasing Λ for any L values. Therefore, a nanostructure having both small L and Λ (while L is also much smaller than its Λ) will be the most optimized condition to enhance PF.

Now we can compare our model with various experimental data. In Fig. 3.5, we show $PF_{\rm opt}$ (Eq. (3.12)) as a function of L/Λ for different dimensions (1D, 2D, and 3D systems). The $PF_{\rm opt}$ values are scaled by the optimum power factor of a 3D system, $PF^{\rm 3D}_{\rm opt}$. From Eq. (3.12), we see that the ratio $PF_{\rm opt}/PF^{\rm 3D}_{\rm opt}$ merely depends on L/Λ and D. Hence, PF from various materials can be compared directly with the theoretical curves shown in Fig. 3.5. The experimental data in Fig. 3.5 are obtained from the PF values of 1D Bi nanowires [11], 1D Si nanowires [10], 2D Si quantum wells [44], and two different experiments of 2D PbTe quantum wells labeled by PbTe–1 and PbTe–2 [45, 46]. Here we use fixed parameters for the thermal de Broglie wavelength of each material: $\Lambda_{\rm Bi} = 32$ nm, $\Lambda_{\rm Si} = 4.5$ nm, and $\Lambda_{\rm PbTe} = 5$ nm. We also set some PF values for 3D systems: $PF^{\rm 3D}_{\rm Bi} = 0.002$ W/mK^2 [11], $PF^{\rm 3D}_{\rm Si} = 0.004$

Fig. 3.5: Fig/chapter3-fig5.pdf

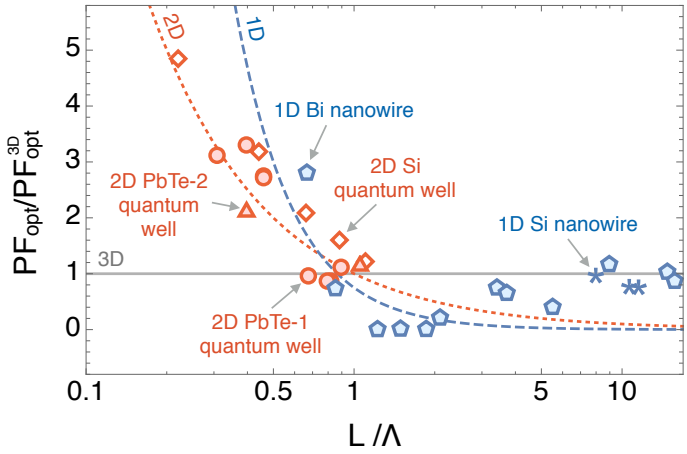

Figure 3.5: $PF_{\rm opt}/PF^{\rm 3D}_{\rm opt}$ as a function of L/Λ for different dimensions. The L/Λ axis is given using a logarithmic scale. Theoretical results for 1D, 2D, and 3D systems are represented by dashed, dotted, and solid lines, respectively. Asterisks, pentagons, diamonds, circles, and triangles denote experimental results for 1D Si nanowires [10], 1D Bi nanowires [11], 2D Si quantum wells [44], 2D PbTe–1 quantum wells [45], and 2D PbTe–2 quantum wells [46], respectively. For the experimental results, we set the thermal de Broglie wavelength of each material as: $\Lambda_{\rm Bi} = 32$ nm, $\Lambda_{\rm Si} = 4.5$ nm, and $\Lambda_{\rm PbTe} = 5$ nm. We also have the following PF values for 3D systems: $PF^{\rm 3D}_{\rm Bi} = 0.002$ W/mK^2 [11], $PF^{\rm 3D}_{\rm Si} = 0.004$ W/mK^2 [47], $PF^{\rm 3D}_{\rm PbTe-1} = 0.002$ W/mK^2 [45], and $PF^{\rm 3D}_{\rm PbTe-2} = 0.003$ W/mK^2 [46].

W/mK^2 [47], $PF^{\rm 3D}_{\rm PbTe-1} = 0.002$ W/mK^2 [45], and $PF^{\rm 3D}_{\rm PbTe-2} = 0.003$ W/mK^2 [46], which are necessary to put all the experimental results into Fig. 3.5.

We find that the curves in Fig. 3.5 demonstrate a strong enhancement of $PF_{\rm opt}$ in 1D and 2D systems when the ratio L/Λ is smaller than unity (or $L < \Lambda$). In contrast, if L is larger than Λ, the bulk 3D semiconductors may give a larger $PF_{\rm opt}$ value than the lower dimensional semiconductors, as shown in Fig. 3.5 up to a limit of $L/\Lambda \approx 2$. We argue that such a condition is the main reason why an enhanced PF is not always observed in some materials although experimentalists have reduced the size of material. For example, in the case of 1D Si nanowires, where we have $\Lambda_{\rm Si} \sim 4.5$ nm, we can see that the experimental PF values in Fig. 3.5 are almost the same as the $PF^{\rm 3D}_{\rm opt}$. The reason is that the diameters (supposed to represent L) of the 1D Si nanowires, which were about 36–52 nm in the previous experiments [9, 10], are still too large compared with $\Lambda_{\rm Si}$. It might be difficult for experimentalists to obtain a condition of $L < \Lambda$ for the 1D Si nanowires. In the case of materials having larger Λ, e.g., Bi with $\Lambda_{\rm Bi} \sim 32$ nm, the PF values of the 1D Bi nanowires can be enhanced at $L < \Lambda$, which is already possible to achieve experimentally [11]. Furthermore, when $L \gg \Lambda$, it is natural to expect that $PF_{\rm opt}$ of 1D and 2D semiconductors resemble $PF^{\rm 3D}_{\rm opt}$ as shown by some experimental data in Fig. 3.5. It should be noted that, within the one-band model, we do not obtain a smooth transition of $PF_{\rm opt}$ in Fig. 3.5 from the lower dimensional to

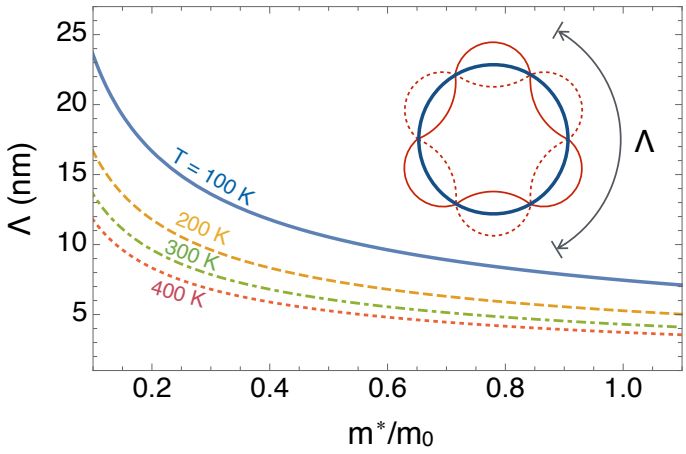

Figure 3.6: Thermal de Broglie wavelength as a function of effective mass m^*/m_0 (m_0 is the mass of a free electron) for several different temperature values.

the 3D characteristics for large L because we neglect contributions coming from many other subbands responsible for the appearance of the 3D density of states [42].

So far, we have used the confinement length L as an independent parameter in Eq. (3.12). However, for extremely thin films or nanowires, L is expressed by two components as $L = L_0 + \Delta L$, where L_0 is the thickness of the material and ΔL is the size of the evanescent electron wavefunction beyond the surface boundary. Within the box of L_0 the electron wavefunction is delocalized, approximated by the linear combination of plane waves, while within ΔL the electron wavefunction is approximated by evanescent waves. For a single-layered material, e.g., a hexagonal boron nitride (h-BN) sheet, $L_0 \approx 0$ so that $L \approx \Delta L = 0.333$ nm [48]. As for ultra-thick 1D nanowires or 2D thin films, we have $L \gg \Delta L$, and thus the confinement length is mostly determined by the size of the material such as $L \approx L_0$. Creating a 1D channel from a 2D material by applying negative gate voltages on two sides of the 2D material can be an example to engineer the confinement length [49]. However, unlike L, which can be controlled by engineering techniques within the same material, the thermal de Broglie wavelength Λ is temperature-dependent and intrinsic for each material. As shown in Fig. 3.6, we can see that Λ decreases ($\propto T^{-1/2}$ or $m^{*-1/2}$) with increasing temperature T or with increasing effective mass m^*, which indicates that the PF_{opt} [$\propto (L/\Lambda)^D$] of nondegenerate semiconductors would be enhanced at higher T or at larger m^* (smaller Λ). This result is consistent with the experimental observations for the PF values of Si and PbTe, which are monotonically increasing as a function of temperature [10, 47, 50]. It should be noted that Λ is not necessarily independent of L and D because the term m^* may be altered by varying L or by changing D.

Fig. 3.6: Fig/chapter3-fig6.pdf

This fact might contribute to the small discrepancy between the PF values from our theory and those from experiments since we set Λ as a fixed quantity upon variation of L in 1D and 2D systems (see Fig. 3.5). For the 3D system, the theoretical values ($PF_{\mathrm{Bi}}^{\mathrm{3D}} = 0.0019$ W/mK^2 and $PF_{\mathrm{Si}}^{\mathrm{3D}} = 0.0044$ W/mK^2) are in good agreement with the experimental data ($PF_{\mathrm{Bi}}^{\mathrm{3D}} = 0.002$ W/mK^2 [11] and $PF_{\mathrm{Si}}^{\mathrm{3D}} = 0.004$ W/mK^2 [47]).

Chapter 4

Thermopower of semiconducting single wall carbon nanotubes

In this Chapter, we show the thermopower (or Seebeck coefficient) of many semiconducting single wall carbon nanotubes (s-SWNTs) by using the Boltzmann transport formalism combined with an extended tight-binding model. We also derive an analytical formula to reproduce the numerical calculation of the thermopower and we find that the thermopower of a given s-SWNT is directly related with its energy band gap. The formula explains the dependence of the thermopower as a function of tube diameter. We find that the thermopower of s-SWNTs increases with decreasing the tube diameter. The large thermopower values may be attributed to the one dimensionality of the nanotubes and to the presence of large energy band gaps of the small-diameter s-SWNTs.

4.1 Model and computational details

To utilize the single wall carbon nanotubes (s-SWNTs) as a main material in future thermoelectric devices, we consider a model shown in Fig. 4.1, in which two identical s-SWNTs, one with p-type and the other with n-type doping, are connected in parallel. Each s-SWNT should maintain its electronic charge distribution in the nonequilibrium state, for example, by a temperature gradient along the tube axis. By having their temperature gradient ∇T from an edge of each s-SWNT to its other edge, charge carriers (electrons or holes) will flow with velocity v from the hot edge with temperature $T_{\rm hot}$ to the cold edge with temperature $T_{\rm cold}$. The carrier distribution f_0, which depends on the electronic energy ε and chemical potential μ, is modified as a function of ε, following the Boltzmann transport formalism. Within such a process, an electric voltage ∇V can be generated. It is also known from earlier studies that the

Fig. 4.1: Fig/chapter4-fig1.pdf

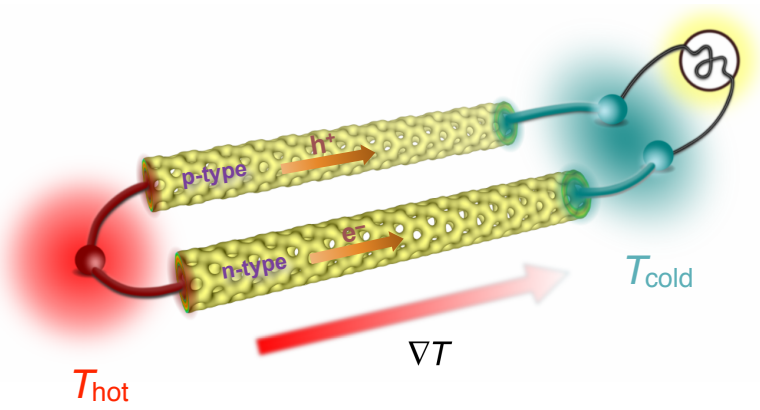

Figure 4.1: Schematic model of a thermoelectric device using two identical s-SWNTs, one with p-type and the other with n-type doping. The temperature gradient between the two edges of each nanotube generates an electric current.

electron-phonon interaction is the main factor determining the electrical conductivity of SWNTs [51, 52, 53], in which the so-called twisting (TW) phonon mode with a long wavelength gives the dominant contribution to the electron-phonon interaction. In particular, Jiang et al. showed that the relaxation time from the electron scattering with the TW phonon mode is independent of the electron energy [53]. Therefore, here we make the assumption that the thermopower from the Boltzmann transport equation can be obtained by applying the relaxation time approximation (RTA) and we may even treat the relaxation time as a constant. Under the RTA, the thermopower or Seebeck coefficient S is expressed by Eq. (2.93) (see in Chapter 2)

$$S = \frac{1}{qT} \frac{\int q\mathbf{v}\tau\mathbf{v} \dfrac{\partial f_0}{\partial E}(E-\mu)g(E)\mathrm{d}E}{\int q\mathbf{v}\tau\mathbf{v} \dfrac{\partial f_0}{\partial E} g(E)\mathrm{d}E}. \tag{4.1}$$

where $q = \pm e$ is the unit carrier charge, $T = (T_{\mathrm{hot}} + T_{\mathrm{cold}})/2$ is the average absolute temperature, $\mathbf{v}$ is the carrier velocity, τ is the carrier relaxation time, $g(E)$ is the density of state (DOS), and μ is the chemical potential.

We employ both numerical and analytical methods to obtain S from Eq. (4.1). In the full numerical approach, we can use the BoltzTraP code [54], which is a widely-used package to calculate some thermoelectric properties, such as the thermopower and electrical conductivity. A necessary input for the BoltzTraP code is the electronic energy dispersion $E(\mathbf{k})$ for all bands (multiband structure) (see in Appendix B). The BoltzTraP code also adopts a constant τ, which is fitted to the case of s-SWNTs. While the BoltzTraP code is actually sufficient for obtaining the thermopower from Eq. (4.1), we cannot discuss the physics of the thermopower of s-SWNTs without having an

explicit formula for the thermopower that depends on some physical parameters, such as the SWNT energy band gap and geometrical structure. Therefore, we also solve Eq. (4.1) analytically by considering the valence band and the conduction band closest to the Fermi level, known as the two-band model [13, 55]. The derivation of the analytical formula is explained in detail in Chapter 2.

As the input for the BoltzTraP code, we calculate the energy dispersion $E(\mathbf{k})$ within the extended-tight binding (ETB) model which was developed in our group [29]. The ETB model takes into account long-range interactions, SWNT curvature corrections, and geometrical structure optimizations, which are sufficient to reproduce the experimentally observed energy band gaps of the SWNTs [29, 56]. The SWNT structure in our notation is denoted by a set of integers (n, m) which is a shorthand for the chiral vector $\mathbf{C}_h = n\mathbf{a}_1 + m\mathbf{a}_2$ [Eq. (2.51)], where $\mathbf{a}_1$ and $\mathbf{a}_2$ are the unit vectors of an unrolled graphene sheet (see in Chapter 2). The chiral vector $\mathbf{C}_h$ defines the circumferential direction of the tube, giving the diameter d_t. Another vector perpendicular to $\mathbf{C}_h$ defines the tube axis, which is called the translational vector $\mathbf{T}$ [Eq. (2.54)]. The chiral and translational vectors thus represent the tube unit cell. In the BoltzTraP calculation, we use a 20 nm $\times$ 20 nm $\times$ $|\mathbf{T}|$ supercell, where $|\mathbf{T}|$ (in nm) is the length of the translational vector. A large supercell length in the x- and y-directions is chosen so as to guarantee the one-dimensionality of the SWNTs. Since the thermopower in the BoltzTraP code is expressed in terms of a tensor [54], the corresponding thermopower tensor component for a given s-SWNT is S_{zz}, which is the thermopower along the tube axis direction. Other tensor components are negligible.

4.2 Effects of temperature and chemical potential on thermopower of s-SWNTs

In Fig. 4.2, we show a first example of the thermopower calculation result for an $(11, 0)$ s-SWNT. The thermopower (S_{zz}) is plotted versus chemical potential and temperature. We see that the thermopower is higher at the lower temperature because $S \propto 1/T$ in Eq. (4.1). The maximum thermopower obtained for the $(11, 0)$ SWNT is about 1420 μV/K, which is already large for a purely individual s-SWNT compared to that for bundled SWNTs with S of around 100–200 μV/K [21, 23]. Next, we can also plot the thermopower at a specific temperature to see the chemical potential dependence of the thermopower. In Fig. 4.3, we show the thermopower versus chemical potential for three different s-SWNT chiralities: (11, 0), (12, 4), and (15, 5), at T = 300 K. The solid lines in Fig. 4.3 represent the numerical results. For all chiralities, the optimum value of the thermopower, indicated by a maximum (minimum) along the negative (positive) axis of the chemical potential, arises due to the p-type

Fig. 4.2: Fig/chapter4-fig2.pdf

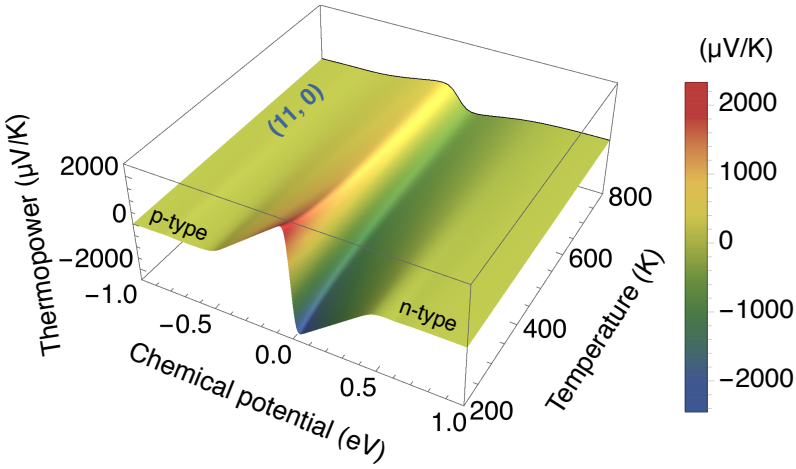

Figure 4.2: Thermopower as a function of chemical potential and temperature for an $(11, 0)$ s-SWNT.

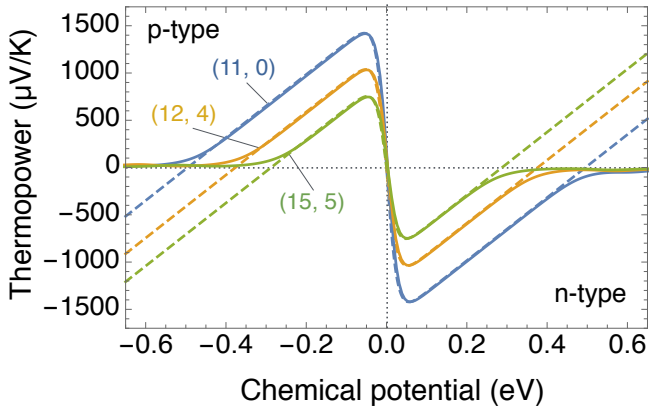

Figure 4.3: Thermopower as a function of chemical potential for (11, 0), (12, 4), and (15, 5) at $T = 300$ K. Solid lines are obtained from the numerical calculation based on Eq. (4.1) while dashed lines are obtained from the analytical formula given in Eq. (4.2).

(n-type) characteristics of the s-SWNTs, which is consistent with a recent experimental observation [23]. The dependence of the thermopower on the chemical potential implies that it is possible to tune the thermoelectric properties of the s-SWNTs by applying a gate voltage, giving p-type and n-type control over the thermopower.

In order to understand the numerical results of thermopower, we have derived an analytical formula for the thermopower within the two-band model [13, 55]. It note that the thermopower is linear function with the chemical potential within only one band, the contribution of two bands is thus required to get the optimum of the

Fig. 4.3: Fig/chapter4-fig3.pdf

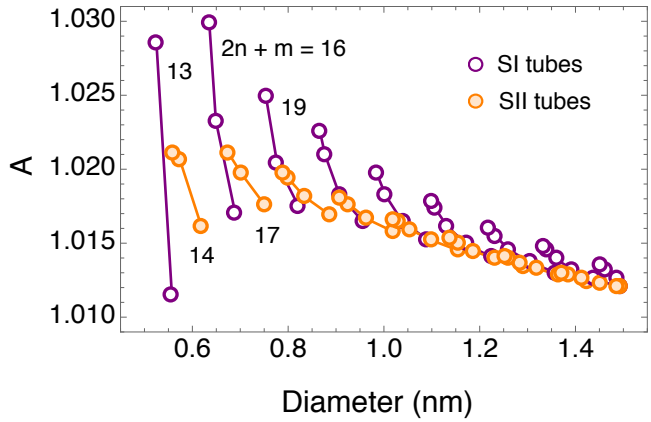

Figure 4.4: Coefficient $A = \left(m_n^*/m_p^*\right)^{-1/2}$ for s-SWNTs plotted as a function of the SWNT diameter. SI and SII tubes correspond to the SWNTs having mod $(2n+m, 3) = 1$ and 2, respectively. Solid lines connect SWNTs with the same $2n+m$ value.

thermopower in the s-SWNTs. In the Chapter 2, the thermopower (or the Seebeck coefficient) S based on two-band model are given by Eq. (2.124) (see Ref. [34])

$$S = \frac{k_B}{e}\left(\frac{\mu}{k_{\rm B}T} - \frac{E_g}{2k_{\rm B}T} - r - \frac{D}{2} - 1 + \frac{E_g/k_{\rm B}T + 2r + D + 2}{Ae^{2\mu/k_{\rm B}T}+1}\right). \tag{4.2}$$

where e is the elementary electric charge, μ is the chemical potential, E_g is the band gap, r is the characteristic exponent which depends on the scattering mechanisms, and $D = 1, 2, 3$ denotes the dimension of the material. The coefficient A is expressed by

$$A = \left(\frac{m_e^*}{m_h^*}\right)^{\frac{D}{2}-1}, \tag{4.3}$$

where m_e^* and m_h^* are the effective masses for electron and hole of conduction band and valence band, respectively.

We now finally have all the information needed to derive the thermopower $S_{\rm CNT}$ of the s-SWNTs. Since s-SWNTs are one-dimensional (1D), we have $D = 1$ and $A = (m_e^*/m_h^*)^{-1/2}$. The electron and hole effective masses $m_{e,h}^*$ in the s-SWNTs can be calculated using the effective mass formula

$$m^* = \hbar^2\left(\frac{{\rm d}^2E}{{\rm d}\mathbf{k}^2}\right)^{-1}, \tag{4.4}$$

where $E(\mathbf{k})$ is the electronic energy dispersion within the extended tight binding (ETB) model [29]. We can obtain A as a function of diameter, as can be seen in Fig. 4.4, in which we show A within a diameter range of 0.5–1.5 nm. In this diameter range, we have $A \approx 1$. With such an approximation, and also assuming that the carrier

Fig. 4.4: Fig/chapter4-fig4.pdf

relaxation time is the constant relaxation time approximation (CRTA) [43] (which gives $r = 0$), the thermopower of s-SWNTs is then given by

$$S_{\rm CNT} = \frac{k_{\rm B}}{e}\left(\frac{\mu}{k_{\rm B}T} - \frac{E_g}{2k_{\rm B}T} - \frac{3}{2} + \frac{E_g/k_{\rm B}T + 3}{e^{2\mu/k_{\rm B}T}+1}\right). \tag{4.5}$$

The E_g values adopted in Eq. (4.5) are obtained from previous ETB results [29]. We note that the reason why we put $r = 0$ is that the electron relaxation time τ in the s-SWNTs is determined mainly by the electron-phonon interaction with the TW phonon mode, where the relaxation time is taken to be independent of the electron energy [53]. Therefore, we can write $\tau \equiv \tau_0$ under the CRTA or equivalently $r = 0$.

The dashed lines in Fig. 4.3 represent the fit of the numerical results of the thermopower using Eq. (4.5) for three different s-SWNT chiralities. The analytical formula [Eq. (4.5)] fits to the numerical results near $\mu = 0$. In particular, the two optimum thermopower values (maximum and minimum for p-type and n-type doping, respectively) can be well-reproduced in that region, which implies that the energy bands near the Fermi level give the strongest contribution to the thermopower of s-SWNTs. The analytical results deviate from the numerical results at larger $|\mu|$ far from the optimum thermopower because the two-band model is no longer valid at a higher doping level. However, for the discussion in this paper, the two-band model is already sufficient to describe the thermopower of s-SWNTs since we will mainly focus on the optimum values of the thermopower.

For a more rigorous argument, we determine a condition to obtain an optimized chemical potential $\mu_{\rm opt}$ from Eq. (4.5), which satisfies

$$\mathrm{d}S_{\rm CNT}(\mu_{\rm opt})/\mathrm{d}\mu = 0. \tag{4.6}$$

We then obtain

$$\mu_{\rm opt} = \frac{k_{\rm B}T}{2}\ln\left(\frac{E_g}{k_{\rm B}T} + 2 \pm \sqrt{\left(\frac{E_g}{k_{\rm B}T}+2\right)^2 - 1}\right), \tag{4.7}$$

where the + and − signs define the n-type and p-type contributions, respectively. From Eq. (4.7), we can say that the $\mu_{\rm opt}$ values will move more distant from $\mu = 0$ as E_g becomes larger than $k_{\rm B}T$, as shown in Fig. 4.5 (a). However, due to the presence of the logarithmic term, $\mu_{\rm opt}$ is very slowly changing as a function of E_g when E_g is much larger than k_BT. This behavior can be seen in Fig. 4.5 (b), in which we show the E_g dependence of $\mu_{\rm opt}$. For the d_t range of 0.5–1.5 nm, the s-SWNTs have E_g values of about 1.58 eV down to 0.46 eV. In this case, E_g is about 17–61 times larger than $k_{\rm B}T$ for $T = 300$ K. With those E_g values, we then obtain $0.046 < |\mu_{\rm opt}| < 0.062$ eV at a constant $T = 300$ K [see Fig. 4.5 (b)], which implies that the change in μ_{opt} in this case is only about 16 meV although the change in E_g is as large as about 1.12 eV for

Fig. 4.5: Fig/chapter4-fig4.pdf

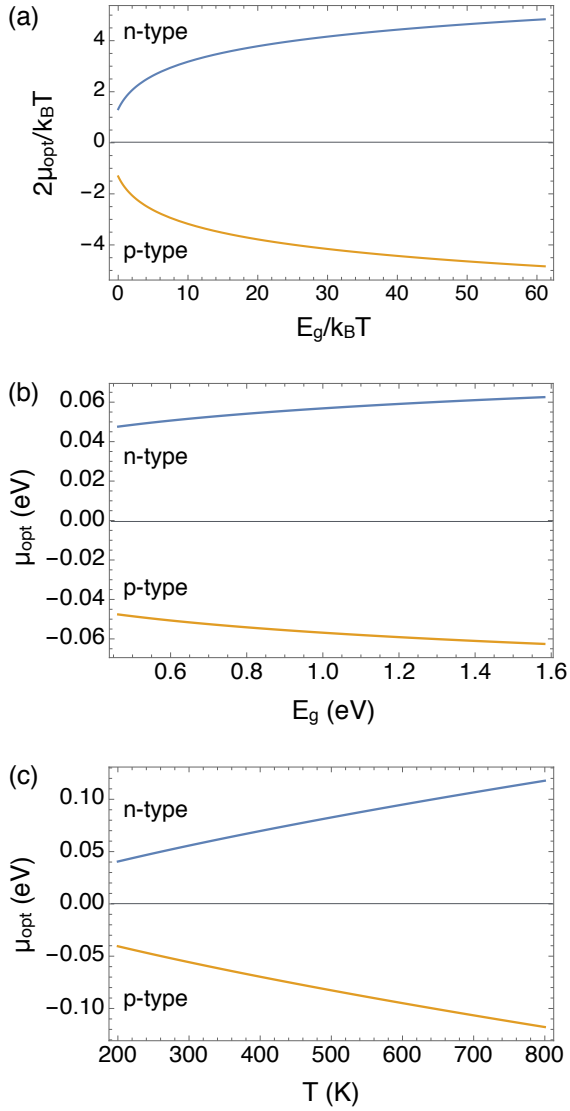

Figure 4.5: The optimized chemical potential $\mu_{\rm opt}$ plotted as a function of the energy band gap of s-SWNTs. In panel (a), we scale the chemical potential and the band gap by $k_{\rm B}T/2$ and $k_{\rm B}T$, respectively, as described by Eq. (4.7). In the case of (b), we set a constant $T = 300$ K and vary E_g, while in (c) we set a constant $E_g = 0.913$ eV, which is the energy band gap value of an (11, 0) s-SWNT, and vary the temperature.

the same d_t range. At room temperature, controlling the doping level or the chemical potential is thus useful to give us the optimum thermopower for the s-SWNTs under consideration. On the other hand, by decreasing T for a given E_g, we can also decrease $\mu_{\rm opt}$, as shown in Fig. 4.5 (c), which is required to obtain the optimum thermopower. It should be noted that in Fig. 4.5 (c) we intentionally set a constant $E_g = 0.913$ eV

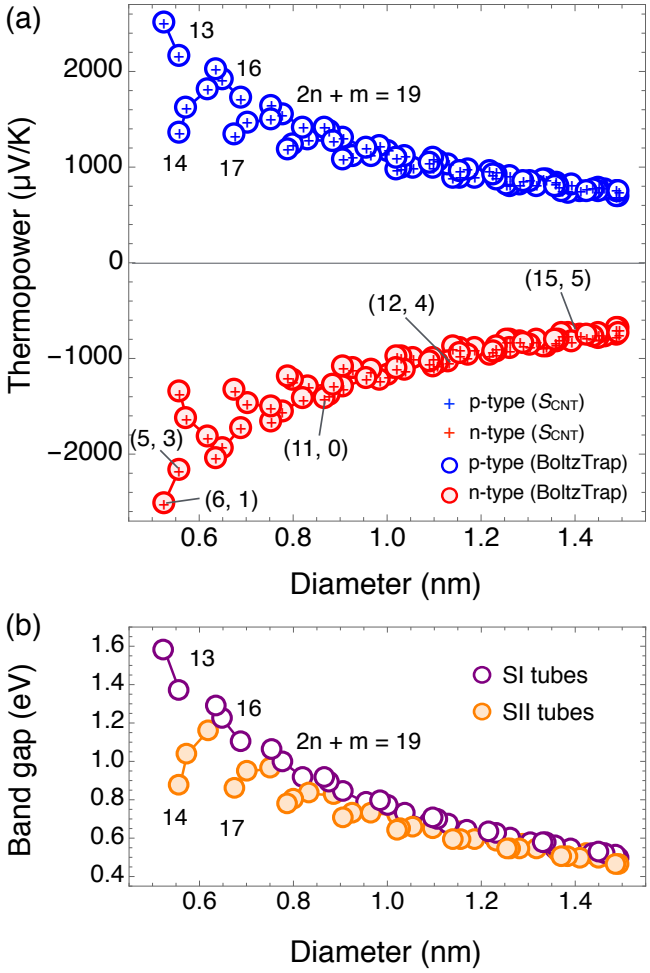

Figure 4.6: (a) Optimum thermopower $S_{\mathrm{CNT}}^{\mathrm{opt}}$ values for all s-SWNTs within the diameter range of 0.5–1.5 nm plotted as a function of SWNT diameter. The temperature is set constant at 300 K. Numerical results from BoltzTraP are denoted by circles, while analytical results from Eqs. (4.2)-(4.7) are denoted by plus symbols. (b) The Kataura plot showing the family pattern of the SWNT band gap as a function of diameter. Solid lines are a guide for the eyes, connecting SWNTs with the same family number $2n + m$. The SI and SII tubes correspond to the SWNTs having $\mod(2n + m, 3) = 1$ and 2, respectively.

for simplicity although the s-SWNT band gaps in the realistic case may decrease as a function of temperature by about 3% when we increase T from 200 K to 800 K [57].

4.3 Diameter-dependent thermopower of s-SWNTs

Fig. 4.6: Fig/chapter4-fig5.pdf

Using both the numerical calculation by BoltzTraP and our analytical formula S_{CNT}, it is now possible for us to plot the thermopower of s-SWNTs over a broad range of d_t by taking the optimum value of the thermopower. In the case of the analytical formula, we define the optimum thermopower $S_{\mathrm{CNT}}^{\mathrm{opt}}$ from Eqs. (4.2) and (4.7), as follows

$$S_{\mathrm{CNT}}^{\mathrm{opt}} = S_{\mathrm{CNT}}(\mu = \mu_{\mathrm{opt}}). \tag{4.8}$$

In Figs. 4.6 (a-b), we show the optimum thermopower values of many s-SWNTs with $0.5 \leq d_t \leq 1.5$ nm compared with their corresponding band gaps as a function of diameter. In Fig. 4.6 (a), we plot the optimum thermopower calculated from the BoltzTrap simulation (denoted by circles) and from $S_{\mathrm{CNT}}^{\mathrm{opt}}$ (denoted by plus symbols) on the same scale. We can see that the two methods show a good agreement. From Fig. 4.6 (a), the thermopower of s-SWNTs is also found to increase as the tube diameter d_t decreases. For some s-SWNTs with $d_t < 0.6$ nm, such as those with $2n + m = 13$, i.e. the (5, 3) and (6, 1) s-SWNTs, the thermopower can reach a value more than 2000 μV/K. These thermopower values are about 6–10 times larger than those found in common thermoelectric materials [9, 10, 20, 58].

The larger thermopower for smaller-diameter s-SWNTs can be explained by the relation of S_{CNT} with E_g as shown in Eq. (4.2) and by the fact that $E_g \propto 1/d_t$ [59]. The one-dimensional character of the SWNT electronic DOS may also enhance the thermopower [7, 8]. Here, we should note that the thermopower of s-SWNTs as a function of diameter shows the nanotube family pattern, in which the different SWNTs with the same $2n + m$ can be connected and they make a clearly distinct branch for mod $(2n + m, 3) = 1$ and mod $(2n + m, 3) = 2$, known as the nanotube SI and SII family branches, respectively [59]. This behavior is very similar to that found in the band gap as a function of diameter shown in Fig. 4.6 (b), which is often referred to as the Kataura plot [59, 33, 30]. This result also suggests that the measurement of the thermopower of a single chirality s-SWNT sample might be able to predict an exact band gap value of the s-SWNT. In fact, the band gap is directly connected to the thermopower as can be seen in the S_{CNT} formula [Eq. (4.2)].

4.4 Comparison between numerical and analytical methods

To verify the accuracy of the $S_{\mathrm{CNT}}^{\mathrm{opt}}$ in fitting the numerical results of the s-SWNT thermopower, we show in Fig. 4.7 the difference of the thermopower obtained from the analytical and numerical calculations in terms of the error percentage. This error percentage variable is defined by the difference in the thermopower calculated by using the $S_{\mathrm{CNT}}^{\mathrm{opt}}$ formula with respect to the numerical results for each s-SWNT diameter. We obtain the error values ranging from -2% to 4% for both p-type and n-type s-SWNTs. The error values increase with the increase of the tube diameter because

Fig. 4.7: Fig/chapter4-fig6.pdf

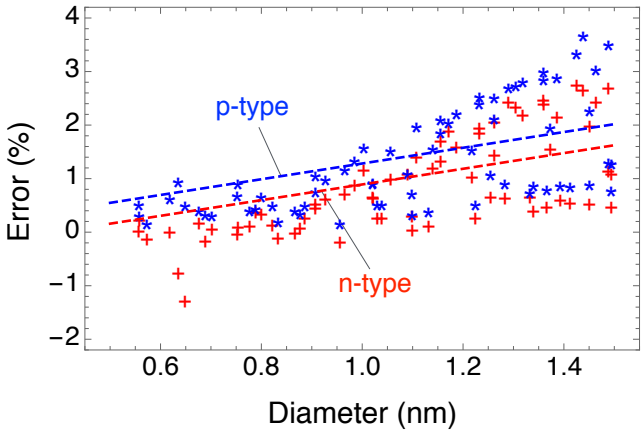

Figure 4.7: The percentage error, or the discrepancy between the analytical and the numerical results of the thermopower calculations for each s-SWNT, is plotted versus the SWNT diameter. The discrepancy increases linearly with increasing the SWNT diameter, as indicated by the fitted dashed lines.

$E_g \propto 1/d_t$ and also because the formula for S_{CNT} [Eq. (4.2)] was derived by assuming s-SWNTs as non-degenerate semiconductors. Therefore, larger band gaps or smaller diameter s-SWNTs should be more accurately fitted by our S_{CNT} approximation.

Chapter 5

Conclusions

In this thesis, we have discussed theoretical calculation for the thermoelectric properties of low-dimensional semiconductors. Calculations have been performed particularly for the thermoelectric power factor of the 1D, 2D, and 3D systems based on the one-band model and the thermopower of individual s-SWNTs with many diameters using the Boltzmann transport formalism combined with the extended tight-binding model. In order to understand the transport properties in thermoelectricity such as the electrical conductivity, the electronic thermal conductivity, and the thermopower, we need a detailed knowledge of the electronic structure, the carrier velocity of the energy band, the relaxation time, and the density of state. In this thesis, we have developed both numerical and analytical calculations for the thermopower and the power factor of low-dimensional semiconductors. Our finding can then be divided into two parts as follows.

Quantum effects on thermoelectric power factor of low-dimensional semiconductors

We have shown that the largest power factor PF values might be obtained for low-dimensional systems by decreasing both the confinement length L and the thermal de Broglie wavelength Λ while keeping $L < \Lambda$. Depending on the dimension of materials, there is a different interplay between L and Λ to enhance the power factor. A simple analytical formula [Eq. (3.12)] based on the one-band model has been derived to describe the quantum effects on the PF in 1D, 2D, and 3D systems. We would suggest to experimentalists to check the trade-off between L and Λ in order to enhance PF for different dimensions of their semiconductors.

Diameter dependence of thermoelectric power of semiconducting carbon nanotubes

We have shown the theoretically predicted behavior of the thermopower of many s-SWNTs within a diameter range of 0.5–1.5 nm. We derive a simple formula to calculate the thermopower of s-SWNTs from their band gap, which enables us to predict the optimum thermopower values. The optimum thermopower value of an individual s-SWNT (p-type or n-type) can be larger than 2000 μV/K at room temperature for diameters less than 0.6 nm, such as the (5, 3) and (6, 1) s-SWNT. Our results highlight potential properties of small diameter s-SWNTs as a one-dimensional thermoelectric material with a giant thermopower. With the recent advances in the fabrication methods for specific small diameter s-SWNTs, we expect that the further potential development of s-SWNT thermoelectric devices could be realized in the near future.

Appendix A

Thermodynamic uncertainty principle

Let us consider an ideal gas moving at random in a trapping potential. We assume that the space of the potential as a container of the volume $V \sim L^D$, where L is the confinement length (or potential size) and $D = 1, 2, 3$ denotes the dimension of the system. The classical system means that the position of the wall in the container is well defined: it is the point at which the particle is reflected back into the container, also known as the classical turning point. On the other hand, in a quantum system, the particle is reflected before reaching the classical turning point or tunnels past the uncertainty principle turning point. That means that L has an uncertainty ΔL due to the uncertainty principle that results in uncertainty of volume ΔV. We can use the law of ideal gas to define the pressure (i.e., the force of gas atoms per unit area) as

$$P = 2p\rho v, \tag{A.1}$$

where p is the component of momentum normal to the wall, ρ is the gas density, v is the averaged velocity of gas, and ρv is the number of collisions. In quantum mechanics, the Heisenberg's uncertainty principle is explained as

$$\Delta p \Delta L \geq \frac{\hbar}{2}, \tag{A.2}$$

where $\hbar$ is the Planck constant. After substituting Eq. (A.1), the Eq. (A.2) can be rewritten as

$$\Delta P \Delta L \geq \hbar \rho v. \tag{A.3}$$

Since the equations of state for the ideal gas is expressed as $PV = Nk_{\mathrm{B}}T$, where N is the total number of particles, T is the temperature of the gas, and k_{B} is the Boltzmann constant, the gas density can take the form $\rho = P/k_{\mathrm{B}}T$. In addition, the velocity of the particle in the Boltzmann distribution can be given as

$$v^2 = \frac{Dk_{\mathrm{B}}T}{m^*}, \tag{A.4}$$

where m^* is the effective mass of the particle. Inserting these quantities into Eq. (A.3) gives

$$\frac{\Delta P}{P}\frac{\Delta L}{L} \geq \sqrt{\frac{D}{2\pi}}\frac{\Lambda}{L}, \tag{A.5}$$

where $\Lambda = (2\pi\hbar^2/k_{\mathrm{B}}Tm^*)^{1/2}$ is defined by the thermal de Broglie wavelength of a particle. Since the volume V is proportional to L^D, then we get

$$\frac{\Delta P}{P}\frac{\Delta V}{V} \geq \frac{D^{3/2}}{\sqrt{2\pi}}\frac{\Lambda}{L}, \tag{A.6}$$

This is the generalized thermodynamic uncertainty principle for an ideal gas. This means that when L is comparable with Λ, $L \leq (D^{3/2}/\sqrt{2\pi})\Lambda$, the pressure and the volume cannot be treated as commuting observable. In other words, the system becomes the quantum system.

Appendix B

Calculation programs

There are several programs used to perform the thermoelectric calculation. All the necessary programs can be found under the following directory in `FLEX` workstation:

`~nguyen/for/00master/`

Hereafter, this directory will simply be referred to as ROOT/ directory. More detailed explanations about how to use the programs are given in the `00README` file in each subdirectory of `ROOT`.

BoltzTraP code

Directory: `ROOT/boltztrap-1.2.5/`

Main Program: `BoltzTraP.F90`

Boltzmann Transport Properties (BoltzTraP) [54] is a program for calculating the semi-classic transport coefficients. It can be obtained from `www.icams.de/boltztrap`. Here we use BoltzTraP v1.2.5 to calculate the thermopower of a single s-SWNTs with many diameters.

BoltzTraP uses several input and output files:

Input :

- IN.intrans: Input parameters.
- IN.struct: The lattice geometry and point group elements.
- IN.energy: Energy eigenvalues on a **k**-mesh.

Output :

- OUT.transdos: Density of states (DOS).

- OUT.engre: Interpolated eigenvalues.

- OUT.condtens: Thermopower S (V/K), electrical conductivity σ/τ (1/(Ωms)), and electronic thermal conductivity κ_e (W/(mKs)) tensors are written as a function of chemical potential μ (Ry) and temperature T (K).

Extended tight-binding model

Directory: `ROOT/ETB-band/`

Main Program: `ETB-band.f90`

This program calculates the electronic structure of s-SWNTs within the extended tight-binding method and it also makes the input files for the BoltzTraP code.

Input :

- $(m,\ m)$: The integer indices of SWNT (see Eq. (2.51) in Chapter 2).

Output :

- CNT.intrans: Input parameters of SWNT for the BoltzTraP code.

- CNT.struct: The lattice geometry and point group elements of CNT.

- CNT.energy: Energy eigenvalues on a **k**-mesh in the format of the BoltzTraP code.

Mathematica notebooks

We use Mathematica software to plot utilities for some analytical formula in the one-band and the two-band models.

Power factor

Directory: `ROOT/math/powerfactor`

Main Program: `PF-LG.nb, G-m.nb`

`PF-LG.nb` is the mathematica code for plotting Figs. 3.3, 3.4, and 3.5, respectively, in Chapter 3. `G-m.np` is the mathematica code for plotting Fig. 3.6 in Chapter 3.

Thermopower

Directory: `ROOT/math/thermopower`

Main Program: `cnt11-0-3D.nb, thermo-cnt-etb.nb, mass-A.nb, opt.nb, thermopower-full.nb`

`cnt11-0-3D.nb, thermo-cnt-etb.nb, mass-A.nb, opt.nb, thermopower-full.nb` are the mathematica codes for plotting Figs. 4.2, 4.3, 4.4, and 4.5, respectively, in Chapter 4.

Publication list

Journals

(1) N. T. Hung, E. H. Hasdeo, A. R. T. Nugraha, M. S. Dresselhaus and R. Saito, "Quantum effect in the thermoelectric power factor of low-dimensional semiconductors", *Phys. Rev. Lett.* **117** (2016) 036602.

(2) N. T. Hung, D. V. Truong, V. V. Thanh and R. Saito, "Intrinsic strength and failure behaviors of ultra-small single-walled carbon nanotubes", *Comput. Mater. Sci.* **114** (2016) 167-171.

(3) N. T. Hung, A. R. T. Nugraha, E. H. Hasdeo, M. S. Dresselhaus and R. Saito, "Diameter dependence of thermopower of semiconducting carbon nanotubes", *Phys. Rev. B* **92** (2015) 165426.

(4) N. T. Hung and D. V. Truong, "Ab initio study of structural transition and pseudoelasticity in Cu nanowires", *Surf. Sci.* **641** (2015) 1-5.

Conferences

- N. T. Hung, A. R. T. Nugraha and R. Saito, "Themoelectricity of low-dimensional semiconductors", *ATI 2016 Nano Carbon Zao meeting*, 19-21/7/2016, Sendai, Japan.
- N. T. Hung, A. R. T. Nugraha and R. Saito, "An atlas of thermoelectric power of semiconducting carbon nanotubes", *The 49th Fullerenes-Nanotubes-Graphene General Symposium*, 7-9/12/2015, Kyushu, Japan.
- N. T. Hung and R. Saito, "Thermoelectric power of carbon nanotubes from first principles", *The 48th Fullerenes-Nanotubes-Graphene General Symposium*, 21-23/2/2015, Tokyo, Japan.
- N. T. Hung, V. V. Thanh, D. V. Truong and R. Saito, "Strength of ultra-small carbon nanotubes: a density functional theory study", *Proc. XIIth Vietnam Nat. Conf. Solid Mech.* (2015) pp.723-729, Danang, Vietnam.

Bibliography

[1] Lawrence Livermore National Laboratory DOEs 2015, (https://flowcharts.llnl.gov/commodities/energy).

[2] J. P. Heremans, M. S. Dresselhaus, L. E. Bell, and D. T. Morelli, Nature Nanotechnol. 8, 471–473 (2013).

[3] C. B. Vining, Nature Mater. 8, 83–85 (2009).

[4] W. Liu, H. S. Kim, S. Chen, Q. Jie, B. Lv, M. Yao, Z. Ren, C. P. Opeil, S. Wilson, C. W. Chu, and Z. Ren, Proc. Natl. Acad. Sci. 112, 3269–3274 (2015).

[5] W. Liu, H. S. Kim, Q. Jie, and Z. Ren, Scripta Mater. 111, 3–9 (2016).

[6] S. K. Yee, S. LeBlanc, K. E. Goodson, and C. Dames, Energy Enviro. Sci. 6, 2561–2571 (2013).

[7] L. D. Hicks and M. S. Dresselhaus, Phys. Rev. B 47, 12727 (1993).

[8] L. D. Hicks and M. S. Dresselhaus, Phys. Rev. B 47, 16631 (1993).

[9] A. I. Boukai, Y. Bunimovich, J. Tahir-Kheli, J. K. Yu, W. A. Goddard Iii, and J. R. Heath, Nature 451, 168–171 (2008).

[10] A. I. Hochbaum, R. Chen, R. D. Delgado, W. Liang, E. C. Garnett, M. Najarian, A. Majumdar, and P. Yang, Nature 451, 163–167 (2008).

[11] J. Kim, S. Lee, Y. M. Brovman, P. Kim, and W. Lee, Nanoscale 7, 5053–5059 (2015).

[12] R. Saito, G. Dresselhaus, and M. S. Dresselhaus, Physical Properties of Carbon Nanotubes (World Scientific, London, 1998).

[13] H. J. Goldsmid, Introduction to Thermoelectricity (Springer-Verlag, Berlin Heidelberg, 2010).

[14] C. B. Vining, Nature 413, 577–578 (2001).

[15] L. D. Hicks, T. C. Harman, X. Sun, and M. S. Dresselhaus, Physical Review B 53(16), R10493 (1996).

[16] A. Majumdar, Science 303, 777–778 (2004).

[17] S. Chen, K. C. Lukas, W. Liu, C. P. Opeil, G. Chen, and Z. Ren, Adv. Energy Mater. 3, 1210–1214 (2013).

[18] Q. Zhang, H. Wang, W. Liu, H. Wang, B. Yu, Q. Zhang, Z. Tian, G. Ni, S. Lee, K. Esfarjani, G. Chen, and Z. F. Ren, Energy Enviro. Sci. 5, 5246–5251 (2012).

[19] S. Lee, K. Esfarjani, T. Luo, J. Zhou, Z. Tian, and G. Chen, Nature Commun. 5, 3525 (2014).

[20] B. Poudel, Q. Hao, Y. Ma, Y. Lan, A. Minnich, B. Yu, X. Yan, D. Wang, A. Muto, D. Vashaee, X. Chen, J. Liu, M. S. Dresselhaus, G. Chen, and Z. Ren, Science 320, 634–638 (2008).

[21] J Hone, I. Ellwood, M. Muno, A. Mizel, M. L. Cohen, A. Zettl, A. G. Rinzler, and R. E. Smalley, Phys. Rev. Lett. 80, 1042 (1998).

[22] J. Hone, M. C. Llaguno, N. M. Nemes, A. T. Johnson, J. E. Fischer, D. A. Walters, M. J. Casavant, J. Schmidt, and R. E. Smalley, Appl. Phys. Lett. 77, 666–668 (2000).

[23] K. Yanagi, S. Kanda, Y. Oshima, Y. Kitamura, H. Kawai, T. Yamamoto, T. Takenobu, Y. Nakai, and Y. Maniwa, Nano lett. 14, 6437–6442 (2014).

[24] A. D. Avery, B. H. Zhou, J. Lee, E. S. Lee, E. M. Miller, R. Ihly, D. Wesenberg, K. S. Mistry, S. L. Guillot, B. L. Zink, Y. H Kim, J. L. Blackburn, and A. J. Ferguson, Nature Energy 1, 16033 (2016).

[25] J. M. Luttinger, Phys. Rev. 102, 1030 (1956).

[26] G. S. Painter and D. E. Ellis, Phys. Rev. B 1, 4747 (1970).

[27] C. L. Kane, Nature 438, 168–170 (2005).

[28] G. Samsonidze. PhD thesis, MIT, 2007.

[29] Ge. G. Samsonidze, R. Saito, N. Kobayashi, A. Grüneis, J. Jiang, A. Jorio, S. G. Chou, G. Dresselhaus, and M. S. Dresselhaus, Appl. Phys. Lett. 85, 5703–5705 (2004).

[30] R. B. Weisman and S. M. Bachilo, Nano Lett. 3(9), 1235–1238 (2003).

[31] S. M. Bachilo, M. S. Strano, C. Kittrell, R. H. Hauge, R. E. Smalley, and R. B. Weisman, Science 298, 2361–2366 (2002).

[32] D. Porezag, T. Frauenheim, T. Köhler, G. Seifert, and R. Kaschner, Phys. Rev. B 51, 12947 (1995).

[33] H. Kataura, Y. Kumazawa, Y. Maniwa, I. Umezu, S. Suzuki, Y. Ohtsuka, and Y. Achiba, Synthetic Met. 103(1), 2555–2558 (1999).

[34] N. T. Hung, A. R. T. Nugraha, E. H. Hasdeo, M. S. Dresselhaus, and R. Saito, Phys. Rev. B 92(16), 165426 (2015).

[35] X. Sun, Z. Zhang, and M. S. Dresselhaus, Appl. Phys. Lett. 74, 4005–4007 (1999).

[36] I. F. Silvera, Am. J. Phys. 65, 570–574 (1997).

[37] M. Lundstrom, Fundamentals of carrier transport (Cambridge University Press, New York, 2009).

[38] J. Zhou, R. Yang, G. Chen, and M. S. Dresselhaus, Phys. Rev. Lett. 107, 226601 (2011).

[39] D. Chattopadhyay and H. J. Queisser, Rev. Mod. Phys. 53, 745 (1981).

[40] W. Zawadzki and W. Szymańska, J. Phys. Chem. Solids 32(6), 1151–1174 (1971).

[41] J. Moon, J. H. Kim, Z. C. Y. Chen, J. Xiang, and R. Chen, Nano Lett. 13, 1196–1202 (2013).

[42] J. E. Cornett and O. Rabin, Phys. Rev. B 84, 205410 (2011).

[43] R. A. Stradling and R. A. Wood, J. Phys. C: Solid State Phys. 3, L94 (1970).

[44] X. Sun, S. B. Cronin, J. Liu, K. L. Wang, T. Koga, M. S. Dresselhaus, and G. Chen. In Proc. 18th Int. Conf. Thermoelectrics, pages 652–655. IEEE, 1999.

[45] T. C. Harman, D. L. Spears, and M. J. Manfra, J. Electron. Mater. 25, 1121–1127 (1996).

[46] L. D. Hicks. PhD thesis, MIT, 1996.

[47] L. Weber and E. Gmelin, Appl. Phys. A 53, 136–140 (1991).

[48] C. Lee, Q. Li, W. Kalb, X. Z. Liu, H. Berger, R. W. Carpick, and J. Hone, Science 328, 76–80 (2010).

[49] Y. Hirayama, T. Saku, and Y. Horikoshi, Phys. Rev. B 39, 5535 (1989).

[50] J. R. Sootsman, H. Kong, C. Uher, J. J. D'Angelo, C.-I. Wu, T. P. Hogan, T. Caillat, and M. G. Kanatzidis, Angew. Chem. 120, 8746 (2008).

[51] H. Suzuura and T. Ando, Phys. Rev. B 65, 235412 (2002).

[52] A. Javey, J. Guo, M. Paulsson, Q. Wang, D. Mann, M. Lundstrom, and H. Dai, Phys. Rev. Lett. 92, 106804 (2004).

[53] J. Jiang, R. Saito, G. G. Samsonidze, S. G. Chou, A. Jorio, G. Dresselhaus, and M. S. Dresselhaus, Phys. Rev. B 72, 235408 (2005).

[54] G. K. H. Madsen and D. J. Singh, Comput. Phys. Commun. 175, 67–71 (2006).

[55] H. J. Goldsmid and J. W. Sharp, J. Electron. Mater. 28, 869–872 (1999).

[56] V. N. Popov, New. J. Phys 6, 17 (2004).

[57] R. B. Capaz, C. D. Spataru, P. Tangney, M. L. Cohen, and S. G. Louie, Phys. Rev. Lett. 94, 036801 (2005).

[58] Y. Pei, X. Shi, A. LaLonde, H. Wang, L. Chen, and G. J. Snyder, Nature 473, 66–69 (2011).

[59] R. Saito, G. Dresselhaus, and M. S. Dresselhaus, Phys. Rev. B 61(4), 2981 (2000).